1-1-2005

Monte Carlo, small angle light scattering, and dynamic light scattering studies of dilute polymer solutions.

Joseph E. McNamara
University of Massachusetts Amherst

MONTE CARLO, SMALL ANGLE LIGHT SCATTERING, AND DYNAMIC LIGHT SCATTERING STUDIES OF DILUTE POLYMER SOLUTIONS

A Dissertation Presented

by

JOSEPH E. MCNAMARA

Submitted to the Graduate School of the
University of Massachusetts Amherst in partial fulfillment
of the requirements for the degree of

DOCTOR OF PHILOSOPHY

September 2005

Department of Polymer Science and Engineering

MONTE CARLO, SMALL ANGLE LIGHT SCATTERING, AND DYNAMIC LIGHT SCATTERING STUDIES OF DILUTE POLYMER SOLUTIONS

A Dissertation Presented

by

JOSEPH E. MCNAMARA

Approved as to style and content by:

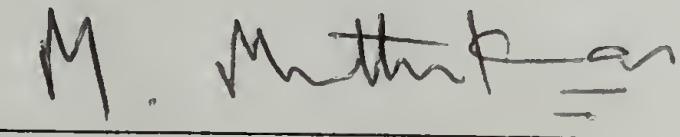

Murugappan Muthukumar, Chair

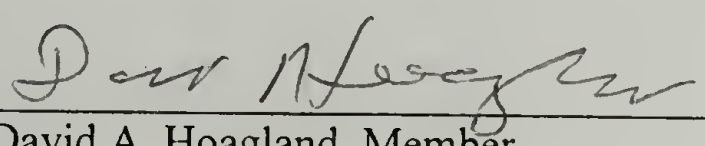

David A. Hoagland, Member

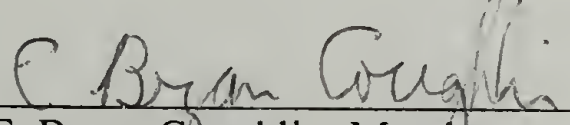

E. Bryan Coughlin, Member

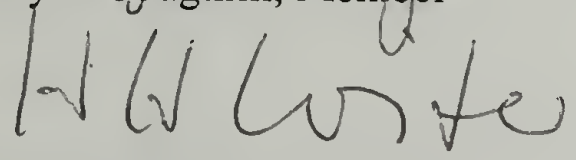

H. Henning Winter, Member

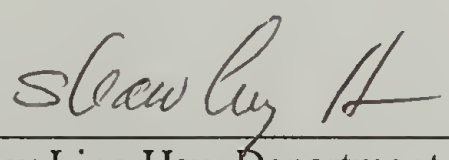

Shaw Ling Hsu, Department Head
Polymer Science and Engineering Department

DEDICATION

I would like to dedicate this thesis to my deceased grandmother Grandma Seibert who always had something nice to say and to my father Joseph R. McNamara who never gave up on me. Also, I would like to impart some advice given to me by my father. He has said many times that the key to success is to have the three d's: desire, discipline and determination. I would also like to thank the rest of my family for being patient and supporting me through the more difficult times of my life.

ACKNOWLEDGMENTS

Acknowledgment is made to the National Science Foundation for support of this research and to the Materials Research Science and Engineering Center at the University of Massachusetts.

ABSTRACT

MONTE CARLO, SMALL ANGLE LIGHT SCATTERING, AND DYNAMIC LIGHT SCATTERING STUDIES OF DILUTE POLYMER SOLUTIONS

SEPTEMBER 2005

JOSEPH MCNAMARA, B.S., WORCESTER STATE COLLEGE

Ph.D., UNIVERSITY OF MASSACHUSETTS AMHERST

Directed by: Professor M. Muthukumar

The adsorption of negatively charged polymer, negative/neutral block copolymer and a polyampholyte to patterned surfaces is investigated using off-lattice Monte Carlo simulations. The surface is decorated by stripe and checkerboard patterns of mixed charges. The polymer has periodic charge segments, which potentially match the periodicity of the surface pattern. Results show that the chain entropy of a flexible polymer disrupts and prevents full pattern recognition. Quantities such as average adsorption energy and the radii of gyration of the adsorbed polymer are calculated and found to be dictated by the size of the surface pattern and its correlation to the polymer charge density. We performed small angle light scattering on dilute-solution-grown polyethylene crystals grown from quenches in *para*-xylene. The quench depths ranged from 60 to 85°C for 0.05 wt.% and 0.1 wt.% linear-low-polydispersity polyethylenes. We found asymmetric scattering patterns for the lower temperature quenches to 65°C, and symmetric scattering patterns for the higher temperature quenches to 80°C. There is a smooth transition from asymmetric to symmetric scattering as we change the quench depth. The correlation lengths $d=2\pi/q_{max}$ corresponding to the peaks of intensity versus q ranged from 15 to 30 μm. We find evidence that these length scales correspond to

assemblies of single polyethylene crystals. Also, we have performed dynamic light scattering on solutions of sodium-poly(styrene-sulfonate) (NaPSS) and poly(ethylene-oxide) (PEO) in water with $BaCl_2$. The fast mode (D_{fast}) and slow mode (D_{slow}) diffusion coefficients were measured as a function of polymer concentration for both polymers in dilute solution. We found that the diffusion coefficients remained relatively constant in the concentration regimes investigated and D_{fast} and D_{slow} for both polymers differed by about 1½ orders of magnitude: 1.1×10^{-6} cm^2/s versus 7.8×10^{-8} cm^2/s for NaPSS and 6.7×10^{-7} cm^2/s versus 4.2×10^{-8} cm^2/s for PEO. Also, we studied more concentrated solutions of PEO without salt and used D_{fast} and D_{slow} to calculate hydrodynamic radii of single and aggregated PEO chains. Using a concentration-dependent viscosity for PEO in water, we found single chain radii from 1 to 5 nm and aggregate radii from 45 to 60 nm.

TABLE OF CONTENTS

Page

ACKNOWLEDGMENTS v

ABSTRACT vi

LIST OF FIGURES x

CHAPTERS

1. INTRODUCTION 1

2. MONTE CARLO STUDIES OF A SEQUENCED POLYELECTROLYTE ADSORBING TO PATTERNED PLANAR SURFACES 6

2.1 Introduction 6
2.2 Model and Simulation Technique 7
2.3 Simulation Results and Discussion 11

2.3.1 Negative Homopolymer 11
2.3.2 Negative-Neutral Block Copolymer 13
2.3.3 Polyampholytes 14

2.4 Summary and Conclusions 16

3. DILUTE POLYETHYLENE CRYSTALLIZATION FROM PARAXYLENE VIA SMALL ANGLE LIGHT SCATTERING 28

3.1 Introduction 28
3.2 Small Angle Light Scattering 31
3.3 Sample Preparation and SALS Procedure 33
3.4 Small Angle Light Scattering Results 36

3.4.1 PE Synthesized In-house 36
3.4.2 NIST PE 0.05 wt.% 38
3.4.3 NIST PE 0.1 wt.% 41

3.5 Summary and Conclusions 43

4. DYNAMIC LIGHT SCATTERING STUDIES OF PEO AND NAPSS AGGREGATION WITH DIVALENT SALT 59

4.1 Introduction 59

4.2 Sample Preparation and Dynamic Light Scattering 61
4.3 Slow Mode and Fast Mode Results 65

4.3.1 120,000 g/mol NaPSS 65
4.3.2 49,000 g/mol PEO 66
4.3.3 PEO Viscosity Calculations 67

4.4 Summary and Conclusions 69

5. SUMMARY AND FUTURE DIRECTIONS 77

5.1 Introduction 77
5.2 Monte Carlo Simulations 77
5.3 Small Angle Light Scattering 78
5.4 Dynamic Light Scattering 79
5.5 Future Directions 80

BIBLIOGRAPHY 82

LIST OF FIGURES

Page

2.1 Various polymers and surfaces modeled in the simulations. Negative homopolymer of length 60, positive/negative block copolymer of length 60, and negative/neutral block copolymer of length 60. Length (x) of alternating blocks of A and B: A_XB_X. Uniform positive surface, stripes of alternating positive and negative or positive and neutral charge, and checkerboards of alternating positive and negative or positive and neutral charge. 18

2.2 Average energy per segment and average radii of gyration squared as a function of stripe and checkerboard size with the negative homopolymer. Average absorption energy per segment for (a) striped surfaces, (b) checkerboard surfaces. Average radii of gyrations squared for (c) striped surfaces, (d) checkerboard surfaces. Open symbols: $\langle R^2(xy)\rangle$ and filled symbols: $\langle R^2(z)\rangle$ 19

2.3 Average adsorption energy per segment as a function of stripe width. Average adsorption energy per segment for negative/neutral block copolymers on striped surface patterns. Alternating negative/neutral polymer blocks of length 6 and 15 with positive/neutral and positive/negative stripes. 20

2.4 Average adsorption energy per segment as a function of negative/neutral polymer block length. Average adsorption energy per segment for negative/neutral block copolymers on checkerboard surfaces for (a) positive/neutral checkerboards of size 3, 5, 6, and 10, (b) positive/negative checkerboards of size 3, 5, 6, and 10. Uniform positive surface also simulated for comparison. 21

2.5 Average radii of gyration squared $\langle R^2(xy)\rangle$ as a function of negative/neutral polymer block length. Average radii of gyrations squared for negative/neutral block copolymers on checkerboard surfaces for (a) positive/neutral checkerboards of size 3, 5, 6 and 10, (b) positive/negative checkerboards of size 3, 5, 6 and 10. Uniform positive surface also simulated for comparison. 22

2.6 Average radii of gyration squared $\langle R^2(z)\rangle$ as a function of negative/neutral polymer block length. Average radii of gyration squared for negative/neutral block copolymers on checkerboard surfaces for (a) positive/neutral checkerboards of size 3, 5, 6 and 10, (b) positive/negative checkerboards of size 3, 5, 6 and 10. Uniform positive surface also simulated for comparison. 23

2.7 Average adsorption energy per segment as a function of positive/negative polymer block length. Average adsorption energy per segment for positive/negative block copolymers on striped surfaces for (a) positive/neutral stripes of size 3, 5 and 10, (b) positive/negative stripes of size 3, 5 and 10. Uniform positive surface also simulated for comparison. 24

2.8 Average radii of gyration squared $\langle R^2(xy)\rangle$ as a function of positive/negative polymer block length. Average radii of gyrations squared for positive/negative block copolymers on striped surfaces for (a) positive/neutral stripes of size 3, 5 and 10, (b) positive/negative stripes of size 3, 5 and 10. Uniform positive surface also simulated for comparison. 25

2.9 Average adsorption energy per segment as a function of positive/negative polymer block length. Average adsorption energy per segment for positive/negative block copolymers on checkerboard surfaces for (a) positive/neutral checkerboards of size 3, 5 and 10, (b) positive/negative checkerboards of size 3, 5 and 10. Uniform positive surface also simulated for comparison. 26

2.10 Average radii of gyration squared $\langle R^2(xy)\rangle$ as a function of positive/negative polymer block length. Average radii of gyrations squared for positive/negative block copolymers on checkerboard surfaces for (a) positive/neutral checkerboards of size 3, 5 and 10, (b) positive/negative checkerboards of size 3, 5 and 10. Uniform positive surface also simulated for comparison. 27

3.1 Schematic of our Small Angle Light Scattering (SALS) system we built for the polyethylene studies. The camera, sample holder, and screen can be moved along a vertical track. A temperature controller is interfaced with the sample holder. A calibration is performed to compensate for the offset position of the camera. 45

3.2 Vertical-vertical (Vv) SALS patterns are shown as a function of time. Intensity versus q is also shown as a function of time. Scattering patterns for 0.05 wt.% PE in *para*-xylene quenched at 65°C. Intensity versus q along the direction depicted with the arrow. The maximum of q is shown for the 10 min. plot and $d = 2\pi/q_{max}$. 46

3.3 Vertical-vertical (Vv) SALS patterns are shown as a function of time. Intensity versus q is also shown as a function of time. Scattering patterns for 0.05 wt.% PE in *para*-xylene quenched at 80°C. Intensity versus q along the direction depicted with the arrow. The maximum of q is shown for the 20 min. plot and $d = 2\pi/q_{max}$. 47

3.4 Absolute transmission of the sample as a function of time. Transmission of main beam for 0.05 wt.% PE in *para*-xylene quenched at 65°C. 48

3.5 Absolute transmission of the sample as a function of time. Transmission of main beam for 0.05 wt.% PE in *para*-xylene quenched at 80°C. 48

3.6 TEM of the quenched crystals after evaporation of the solvent. TEM for 0.05 wt.% PE in *para*-xylene quenched at 65°C. 49

3.7 TEM of the quenched crystals after evaporation of the solvent. TEM for 0.05 wt.% PE in *para*-xylene quenched at 80°C. 50

3.8 Vertical-vertical (Vv) SALS patterns are shown as a function of time. Intensity versus $\boldsymbol{q}$ is also shown as a function of time. Scattering patterns for 0.05 wt.% PE in *para*-xylene quenched at 60°C. Intensity versus $\boldsymbol{q}$ along the direction depicted with the arrow. The maximum of $\boldsymbol{q}$ is shown for the 10 min. plot and $d = 2\pi/q_{max}$. 51

3.9 Vertical-vertical (Vv) SALS patterns are shown as a function of time. Intensity versus $\boldsymbol{q}$ is also shown as a function of time. Scattering patterns for 0.05 wt.% PE in *para*-xylene quenched at 70°C. Intensity versus $\boldsymbol{q}$ along the direction depicted with the arrow. The maximum of $\boldsymbol{q}$ is shown for the 10 min. plot and $d = 2\pi/q_{max}$. 52

3.10 Vertical-vertical (Vv) SALS patterns are shown as a function of time. Intensity versus $\boldsymbol{q}$ is also shown as a function of time. Scattering patterns for 0.05 wt.% PE in *para*-xylene quenched at 75°C. Intensity versus $\boldsymbol{q}$ along the direction depicted with the arrow. The maximum of $\boldsymbol{q}$ is shown for the 20 min. plot and $d = 2\pi/q_{max}$. 53

3.11 Vertical-vertical (Vv) SALS patterns are shown as a function of time. Intensity versus $\boldsymbol{q}$ is also shown as a function of time. Scattering patterns for 0.05 wt.% PE in *para*-xylene quenched at 85°C. Intensity versus $\boldsymbol{q}$ along the direction depicted with the arrow. The maximum of $\boldsymbol{q}$ is shown for the 30 min. plot and $d = 2\pi/q_{max}$. 54

3.12 Vertical-vertical (Vv) SALS patterns are shown as a function of time. Intensity versus $\boldsymbol{q}$ is also shown as a function of time. Scattering patterns for 0.1 wt.% PE in *para*-xylene quenched at 65°C. Intensity versus $\boldsymbol{q}$ along the direction depicted with the arrow. The maximum of $\boldsymbol{q}$ is shown for the 10 min. plot and $d = 2\pi/q_{max}$. 55

3.13. Absolute transmission of the sample as a function of time. Transmission of main beam for 0.1 wt.% PE in *para*-xylene quenched at 65°C. 56

3.14. Vertical-vertical (Vv) SALS patterns are shown as a function of time. Intensity versus q is also shown as a function of time. Scattering patterns for 0.1 wt.% PE in *para*-xylene quenched at 80°C. Intensity versus q along the direction depicted with the arrow. The maximum of q is shown for the 20 min. plot and $d = 2\pi/q_{max}$. 57

3.15 Absolute transmission of the sample as a function of time. Transmission of main beam for 0.1 wt.% PE in *para*-xylene quenched at 80°C. 58

4.1 The The Stokes-Einstein relation for slow mode diffusion coefficient (D_s) and fast mode diffusion coefficient (D_f). A schematic of the slow mode diffusion of aggregates and fast mode diffusion of single chains coupled with sodium, barium and chloride ions. 71

4.2 Diffusion coefficients versus polymer concentration. D_{slow} and D_{fast} values for NaPSS in 0.01M $BaCl_2$ for various polymer concentrations superimposed on data from Förster et al. [44]. 72

4.3 Diffusion coefficients versus polymer concentration. D_{slow} and D_{fast} values for PEO in 0.025M $BaCl_2$ for various polymer concentrations superimposed on data from Förster et al. [44]. 73

4.4 Reduced viscosity of PEO in water and aggregate hydrodynamic radii as a function of PEO concentration. Hydrodynamic radii of 49,000 g/mol PEO aggregates with no added salt calculated with (a) the viscosity of water at 25°C and (b) concentration-dependent viscosity of PEO in water at 25°C. 74

4.5 Reduced viscosity of PEO in water and aggregate hydrodynamic radii versus PEO concentration. Hydrodynamic radii of 96,000 g/mol PEO aggregates with no added salt calculated with (a) the viscosity of water at 25°C and (b) concentration-dependent viscosity of PEO in water at 25°C. 75

4.6 Hydrodynamic radii of single chains as a function of PEO concentration. Hydrodynamic radii of 49,000 g/mol and 96,000 g/mol PEO single chains with no added salt calculated with (a) the viscosity of water at 25°C and (b) concentration-dependent viscosity of PEO in water at 25°C. 76

CHAPTER 1

INTRODUCTION

A polymer solution is dilute when the concentration is low enough so that the interactions between polymers can be neglected. These solutions span from isolated single chains to more concentrated solutions approaching the overlap concentration (c*). Above c*, the solution becomes semi-dilute and the chains interpenetrate making it too concentrated for single chain analysis. This concentration can be calculated using the radius of gyration (R_G), the weight-averaged molecular weight (M_W), and Avogadro's number (N_A):

$$c^* = \frac{M_W}{\frac{4}{3}\pi R_G^3 N_A} \tag{1.1}$$

or, if the Mark-Houwink constants (K, α) and the volume-averaged molecular weight (M_V) are known, from:

$$c^* = \frac{1}{K M_V^{\alpha}} \tag{1.2}$$

The value of c* varies with temperature and the specific polymer/solvent combination.

Dilute polymer solutions are common physical systems and are important in science and industry. These solutions are frequently found in biological systems as components of many extra- and intra-cellular processes and display numerous interesting collective properties including growth of highly ordered crystals and formation of aggregates. Polymers crystallized from dilute organic solvent form isolated single crystals that lack the more complex morphologies of melt-crystallized

polymer. Water-soluble polymers form aggregates with the help of salts and amphiphilic polymers can form micelles. Polymer solutions are used for cosmetics, household products, food processing, and controlling the flow of liquids, among other applications.

We use a combination of computational and experimental techniques to study the physics of dilute polymer solutions. We have performed Monte Carlo simulations of a single polymer chain adsorbing to patterned planar surfaces in aqueous solution. The chain and the surface are decorated with negative, neutral or positive point charges. We calculate the adsorption energy per segment of the polymer and the radii of gyration along the surface. Using Small Angle Light Scattering (SALS) we followed the kinetics of highly linear, low-polydispersity polyethylene crystallizing from dilute solution in *para*-xylene. These studies allowed us to follow the time evolution of scattering as a function of quench depth. We report the scattering data as well as turbidity measurements and TEM of the single crystals. We have also performed Dynamic Light Scattering (DLS) of aqueous solutions of NaPSS and PEO with divalent salt to study aggregation. Measurements were made for both polymers with a fixed amount of salt as a function of polymer concentration. The diffusion coefficients for the single chains as well as aggregates are reported and hydrodynamic radii are calculated.

Our single chain Monte Carlo studies focus on the adsorption of a charged freely jointed polymer onto a planar surface patterned with charge. We study this process by modeling single chain adsorption using a large number of polymer and surface charge-pattern combinations. The modeled polymer has a fixed length and has

either uniform negative charge, negative and neutral alternating blocks or negative and positive alternating blocks of varying length. Our planar surface is a uniform positive grid, alternating positive and neutral or alternating positive and negative patterns of stripes or checkerboards of point charges. The interactions between polymer and surface are modeled as screened electrostatic potentials.

The chain entropy associated with loops in the adsorbed complex prevents efficient adsorption-driven pattern recognition between the polymer and surface. As a result, there is a rugged and hilly free energy landscape with many meta-stable states. Simply increasing the strength of polymer-surface electrostatic interactions does not lead to greater polymer adsorption. We found that polymer-surface interactions must be set just above the adsorption threshold to facilitate complete adsorption. The results indicate that adsorption is stimulated when the charge sequence on the polymer is able to match with a commensurate charge sequence along the surface pattern. Also, adsorption is favored when the charge sequences are longer on both the polymer and surface.

The early stage crystallization of single crystals is generally accepted as a nucleation and growth process, although it is not very well understood. Our goal is to probe the kinetics of crystallization of linear low-polydispersity polyethylene via SALS as a function of quench temperature. We know that crystallization will lead to an increase in overall scattering. Using SALS, we followed the time evolution of scattering and calculated scattering correlation lengths in the micron range.

Our data show that the lower temperature quenches to 65°C result in asymmetric (oval patterns) scattering while the higher temperature quenches to 80°C

result in symmetric (circular patterns) scattering. The transition temperature is between 70 and 75 °C for 0.05 wt.% and 0.1 wt.% polyethylene solutions. The correlation lengths corresponding to maximum scattering are between 15 and 30 μm. These data were produced with an in-house sample of polyethylene and repeated with a higher quality NIST sample and found to be reproducible on our SALS system.

The aggregation of charged polymers with added salt is a well-studied subject. From previous work, we know that a second diffusional mode, known as the slow mode, appears in polyelectrolyte systems as the polymer concentration increases or the ionic strength decreases. It is thought that hydrogen bonding, hydrophobic effects, triple screening, or the presence of impurities gives rise to polymer aggregates, which in turn display slower dynamics. Our goal is to examine dilute aqueous solutions of NaPSS and uncharged PEO with added divalent salt to understand aggregation as a function of polymer concentration. Using Dynamic Light Scattering (DLS) we were able to measure the fast mode and diffusion coefficients for these systems.

We found a consistent slow mode for both NaPSS and PEO with added divalent salt in the polymer concentration regimes investigated. The diffusion coefficients for the single chains as well as the aggregates remained relatively constant in these regimes. These slow mode and fast mode diffusion coefficients differed by about 1½ orders of magnitude for both polymers: 1.1×10^{-6} cm^2/s versus 7.8×10^{-8} cm^2/s for NaPSS and 6.7×10^{-7} cm^2/s versus 4.2×10^{-8} cm^2/s for PEO. Also, we calculated slow mode diffusion coefficients for PEO with no salt. We used these values along with a PEO-concentration-dependent solution viscosity to calculate hydrodynamic radii of PEO using the Stokes-Einstein relation. For 1.25 to 15 g/L of

PEO in water, we found a stable aggregate size of about 50 nm. Using the viscosity of water resulted in a three-fold increase in aggregate size over the same polymer concentration range.

This thesis is divided into three main chapters followed by a summary and future directions chapter. The second chapter is on the Monte Carlo simulations, the third chapter is on the SALS experiments, and the fourth is on the work done on DLS of dilute solutions of NaPSS and PEO. These chapters contain an introductory section describing the problem, a section on the simulation or experimental methods, results and discussion section as well as a conclusions section. In chapter 5, we recount the findings of the previous three chapters and suggest future directions for the extension of our work.

CHAPTER 2

MONTE CARLO STUDIES OF A SEQUENCED POLYELECTROLYTE ADSORBING TO PATTERNED PLANAR SURFACES

2.1 Introduction

The adsorption of a charged polymer at an interface in a solution is a fundamental phenomenon in polymer physics. Differences in surface curvature, charge density and heterogeneity of charges on the surface as well as the nature of the polymer charges will give rise to different binding behaviors [1,2]. This type of adsorption-driven pattern recognition is important in many technological processes [3-7] and has been the subject of extensive experimental investigation [8-15]. Theories have been developed to predict the adsorption criteria for a uniformly charged polymer adsorbing onto uniformly charged planar [16] and curved surfaces [17]. Monte Carlo simulations have supported these theories [18,21-23]. We are interested in the behavior of heterogeneously charged polymers adsorbing to heterogeneously charged planar surfaces.

A set of Monte Carlo simulations is performed to investigate the adsorption behavior of a charged flexible polymer on a patterned flat surface in situations where polymer loops are possible. The polymer can be one of the following: a uniformly charged negative polymer, a negative polymer with neutral blocks (negative/neutral polymer) or a polymer with periodic negative and positive blocks (positive/negative polymer). The surface is a 60×60 grid of neutral, negative or positive point charges that form periodic patterns of stripes or checkerboards. A study of the equilibrium

quantities such as adsorption energy and radii of gyrations perpendicular and parallel to the surface elucidates the conformations of the adsorbed chains.

The most important principle of pattern recognition is entropic frustration leading to a multiplicity of partially adsorbed, meta-stable conformational states of the polymer [19,20]. According to this argument, the entropy associated with loops in the adsorbed complex leads to a rugged and hilly free energy landscape. Thus, the polymer must traverse many meta-stable states to reach the final adsorbed conformation. In order to overcome this entropic frustration, we need to eliminate the possibility of chain loops that interact strongly with the surface and are unlikely to rapidly unfold. This can be accomplished by: (1) reducing the length of the homo-polymer block or (2) reducing the interactions between the surface and polymer to just above the adsorption threshold. In the case of the former, sticky loops are disfavored but pattern recognition is also disrupted. In the case of the latter, we found that tightly bound chain loops can unfold and pattern recognition is favored. Moreover, in our simulations of heterogeneously charged polymers and surfaces, coarse polymer segments and surface patterns enhance adsorption when they are mutually commensurate.

2.2 Model and Simulation Technique

The polymer is represented as a freely jointed chain of $N-1$ bonds of Kuhn length l connecting N beads. The polymer can be uniformly charged with only negative beads, alternating negative and neutral strings of beads or alternating positive and negative strings of beads of equal block length a. Each monomer is ascribed a

hard-core diameter d to account for interactions. The contour length of the chain is $L=N\times l$. Fixing N=60, the values of a=1,2,3,5,6,10,15 and 30 are chosen to give an even number of blocks on the chain as shown in Fig.2.1.

The polymer is confined in a semi-infinite three-dimensional space with an impenetrable planar surface at z=0. The surface is finite and divided into a square lattice of size $60l \times 60l$ with a fixed +1, -1 or 0 charge at the center of each square. The charges on the surface are arranged into patterns as shown in Fig.2.1. Charges on the surface as well as the polymer backbone can be thought of as point charges. The polymer can extend beyond the patterned square lattice, and in that case, that surface is treated as neutral. a characterizes the block sizes of the polymer while b characterizes the size of the surface features. Stripes chosen for the simulations are $b\times 60$, while the squares for the checkerboard patterns are $b\times b$ and the values of b are 3,5,6 and 10. Sizes are chosen so that there is an even number of stripes or squares on the 60×60 grid. For the positive/negative surface patterns, the net charge on the surface is always zero. A uniform positive surface with a +1 at the center of each square is used in some of the simulations for comparison purposes. The simulations for a negative homopolymer and a uniform positive surface were done previously [18].

We assume that the solution, which contains the polymer and surface, can be treated as a continuum with an effective dielectric constant ε at a given temperature T. The ith and jth segments of the chain separated by a distance r_{ij} interact with an excluded volume interaction due to hard-core repulsion:

$$V_1(r_{ij}) = \begin{cases} 0, & r_{ij} > d \\ \infty, & r_{ij} \le d \end{cases} \tag{2.2.1}$$

and through a screened coulomb interaction:

$$V_2(r_{ij}) = k_B T\, q_i\, q_j\, l_B \frac{e^{-\kappa r_{ij}}}{r_{ij}} \tag{2.2.2}$$

where q_i is the charge of the ith bead, q_j is the charge of the jth bead, k_B is the Boltzmann constant, and l_B is the Bjerrum length:

$$l_B = \frac{e^2}{4\pi\,\varepsilon_0 \varepsilon\, k_B T} \tag{2.2.3}$$

with e the electron charge and ε_0 the permittivity of free space. The inverse Debye length, which determines the range of electrostatic interaction, is κ and is given by:

$$\kappa^2 = 4\pi\, l_B \sum_i c_i z_i^2 \tag{2.2.4}$$

where c_i and z_i are the concentration and valence, respectively, of the ith mobile ion. The polymer segments interact with the surface through an excluded volume interaction:

$$V_3(z_i) = \begin{cases} 0, & z_i > d/2 \\ \infty, & z_i \le d/2 \end{cases} \tag{2.2.5}$$

where z_i is the z coordinate of the ith bead of the polymer. The polymer beads also interact with the charges on the lattice through a screened coulomb interaction as in equation (2.2.2) where q_i is the charge on the polymer bead and q_j is the charge on the surface element. The electrostatic interactions are described approximately through these equations as the actual electrostatic potential between a charged polymer and a

charged group of a surface in an ionic solution is unknown at present. The counterions of the polymer and surface and the dissociated salt ions are assumed to be randomly distributed and consequently appear only through the value of the Debye length. The potential used here is sufficient in addressing the generic questions pertinent to the adsorption of a charged polymer on a charged surface pattern. Care should be taken with any quantitative comparison between our results and experimental data.

The basic parameters in this simulation are l, a, b, d, l_B, and κ. The temperature T and the dielectric constant ε appear through the Bjerrum length l_B. In the simulations performed for this study, we fixed l=1, $d/l=3^{1/2}/2$, l_B/l=1/3, κl=0.8, and N=60. The values were chosen to ensure adsorption occurs in most of the simulations, but the interaction is weak enough for polymer mobility along the surface. a and b are the variables in the simulations. There were 288 combinations of polymer and surface pattern simulated four times each.

The chain evolves through a dynamic Monte Carlo algorithm that changes conformation by local motion of segments. A segment chosen at random is rotated through an angle α about the axis defined by adjacent segments to a new trial position. If the chosen segment lies at either end of the chain, it is moved through two randomly chosen angles β and γ to a new trial position (for details, see Ref. [24]). Appropriate statistical weights are assigned to the new conformation and the move is either accepted or rejected via standard Metropolis rules. The attempts are accepted if the beads do not interpenetrate the surface or other beads and if (1) the energy is lower, or if (2) $\exp[-(V_{new}-V_{old})/k_BT] > \Gamma$, where $0 \leq \Gamma \leq 1$ is a uniformly-distributed random number. V is the total of all the bead-bead and bead-surface interactions.

Whether or not the move is accepted, each move is counted as a step. N=60 such elementary steps compose one Monte Carlo time step.

The simulation is carried out as follows. First, we create the polymer with a given charge sequence and the surface with a chosen pattern. Second, the polymer chain is equilibrated in the absence of a surface using the above-mentioned procedure for 10^5 Monte Carlo time steps. Next, the polymer is translated so that its center-of-mass is above the center of the surface and the closest monomer is at a distance of $5l$. The Monte Carlo clock is reset to zero. Then the polymer and the surface are equilibrated for 10^6 Monte Carlo time steps. The absorption energy per segment $<E_s>$ and the radii of gyration perpendicular $<R_g(z)>$ and parallel $<R_g(xy)>$ to the surface are averaged over the 10^6 Monte Carlo time steps. Each polymer and surface pattern combination is repeated with a different random seed for the random number generator. Due to the large number of polymer-surface combinations and limited computational time, the final data are averaged from four sets of repeated simulation runs.

2.3 Simulation Results and Discussion

2.3.1 Negative Homopolymer

We first consider the adsorption of a negatively charged homopolymer onto the patterned surfaces. The average adsorption energy per segment $<E_s>$ is plotted against the characteristic size of the surface patterns b in Figs. 2.2(a) and 2.2(b). $<E_s>$ decreases (i.e., more adsorption) with b for both positive/negative and positive/neutral

surfaces. This is because the larger positive regions accommodate the negatively charged homopolymer more easily. The values of $<E_s>$ are consistently lower for the positive/neutral surfaces shown in Figs. 2.2(a) and 2.2(b). It is due to the absence of negative charges on the surface, which would repel the polymer. The pattern shape also affects the adsorption energy of the polymer. Stripe patterns have lower values of $<E_s>$ than the checkerboard patterns. This is again due to charge accommodation: the stripe pattern is larger than a checkerboard pattern for the same value of b.

The radii of gyration perpendicular and parallel to the surface can characterize the conformations of the adsorbed polymer chain. The radii of gyration values are plotted against b in Figs. 2.2(c) and 2.2(d). When $b < 5$, the $<R^2(\mathrm{xy})>$ of the adsorbed polymer is larger on positive/neutral stripes as shown in Fig. 2.2(c). Starting from $b = 5$, the $<R^2(\mathrm{xy})>$ of the adsorbed polymer is larger on the positive/negative stripes. This is because the positive/negative stripe pattern appears as a neutral surface to the polyanion when the stripe width is small compared to the size of the polymer. The polymer can only adsorb onto the positive/neutral surface. When the positive/negative stripes are wide enough, the polymer stays confined within a single positive stripe. The electrostatic repulsion from the neighboring negatively charged stripes keeps the polyanion on the positive stripe. As a result, the average $<R^2(\mathrm{xy})>$ is larger for the positive/negative stripes than for positive/neutral stripes. For the stripe patterns, there is a slight decrease in $<R^2(\mathrm{xy})>$ from stripe width 6 to 10. This is because, the larger stripe is wide enough for the polymer to bend considerably within it and the effective length of the chain is then less. For checkerboard patterns, the polymer chain adopts a flatter conformation on the surface with increasing b as shown in Fig. 2.2(d).

2.3.2 Negative-Neutral Block Copolymer

We now proceed to consider the adsorption of a polyanion with periodic neutral spacers onto surfaces with stripes. The polyanions used in these simulations contained alternating negatively charged and neutral regions of block lengths a. For a = 6 and 15, $\langle E_s \rangle$ is plotted against the pattern size b in Fig. 2.3. When the polymer is adsorbed onto the surfaces, $\langle E_s \rangle$ monotonically decreases with increasing pattern size b. $\langle E_s \rangle$ is also consistently lower for the positive/neutral stripes than for the positive/negative stripes. Both results are similar to the results obtained from the homogeneously charged polyanion, but $\langle E_s \rangle$ is weaker in both cases than results from the last section. Adding neutral spacers weakens the polymer–surface interaction by reducing the charge correlation of the polyanion.

We continue to examine the effects of changing correlation of the polymer charges on the adsorption behavior. In Figs. 2.4(a) and 2.4(b), we plot $\langle E_s \rangle$ versus block length of the polymer, a, for checkerboard patterns. The results for a homogeneously charged surface are also shown for comparison. For all checkerboard sizes, our results show that $\langle E_s \rangle$ decreases (i.e., more adsorption) with increasing block length for a certain threshold value of a. We observe a non-monotonic dependence of $\langle E_s \rangle$ on a for small values of a in the case of positive/neutral surfaces. This might be within the inherent noise of Monte Carlo simulations on finer patterned grids. Further simulations on patterned surface with smaller blocks are needed. $\langle E_s \rangle$ is again lower for the positive/neutral surface than for the positive/negative surface, but the homogeneous positively charged surface adsorbed the polyanion better than any of

the eheekerboard patterns. This surfaee adsorbed even the shortest polymer block length of $a = 1$. Thcse results show that the polymer–surfaee interactions are eontrolled mainly by the block sizes of the polymer and of the surfacc features.

$<R^2(xy)>$ of the adsorbed polymer is plottcd against the block length a of the polymer in Figs. 2.5(a) and 2.5(b). Typically, the size of the eheckerboard patterns does not significantly change the polymer conformation parallel to the surfacc. For both surfaee patterns of size $b = 10$, the values of $<R^2(xy)>$ pcak at $a = 15$. For small values of b, the polymer can only weakly adsorb onto the surfaccs and $<R^2(xy)>$ of the polymer is small. When b increases, the polymer tries to maximize the polymer–surfaee eontaet by forming multiple contaets with regions on the surface. Thc polymer is stretehed and $<R^2(xy)>$ initially increases with inereasing b. Beyond certain value of b, the polymer eannot stretch anymore beeause of entropie penalty. In order to minimize the free energy, the polymer just stays within one attraetive region and the effeetive length of the polymer reduces. As a rcsult, $<R^2(xy)>$ appcars to peak at $a =$ 15.

$<R^2(z)>$ of the adsorbed polymer is plotted against a in Figs. 2.6(a) and 2.6(b). The results show that ehanging the pattern size has only a very weak effeet on $<R^2(z)>$.

2.3.3 Polyampholytes

We also eonsider the adsorption of a polyampholyte. Wc begin our investigation by studying a single polyampholyte adsorbing onto eharged stripe patterns. The average adsorption energy per segment $<E_s>$ is plotted against a in Figs.

2.7(a) and 2.7(b). $<E_s>$ is shown for a positive homogeneous surface is shown for comparison. Our results show that adsorption begins to occur around $a = 5$. When adsorption occurs, $<E_s>$ monotonically decreases with increasing a. For stripe width $b = 3$, the polyampholyte prefers the positive/neutral surface to the positive/negative surface. For stripe widths $b > 3$, the adsorption favors the positive/negative surface. When the stripe width b of a positive/neutral surface is small relative to a, the polymer sees only an average charge density of the stripes. To the polyampholyte, a positive/neutral surface is effectively positive and a positive/negative surface is effectively neutral. When $b \leq a$, the charges on the polymer can bind to larger regions of attractive potential. The polyampholyte prefers positive/negative surfaces because the surface charges can compensate the mixed charges on the polymer. In the case of $b = 10$, adsorption of a polyampholyte onto positive/negative stripe patterns is even stronger than adsorption onto positive homogeneous surfaces.

$<R^2(xy)>$ of the adsorbed polymer on stripe patterns is plotted against a in Figs. 2.8(a) and 2.8(b). When a is small, $<R^2(xy)>$ is inherently noisy for all stripe widths b as mentioned in the previous section. Above a certain threshold value of a, the size of the polymer is larger when the adsorption is stronger and vice versa. As mentioned previously, the non-monotonic dependence seen in b for $a = 10$ might be due to the inherent noise in our Monte Carlo simulations.

For checkerboard patterns, $<E_s>$ and $<R^2(xy)>$ are plotted against a in Figs. 2.9 and 2.10, respectively. Similar to the stripes, the polyampholyte prefers the positive/negative surfaces to the positive/neutral surfaces. Polymer–surface interaction increases with increasing block length of the polymer charges a and the pattern size b.

To summarize, our basic finding are that long runs of charged polymer blocks will enhance pattern recognition for polyampholytes if commensurate with the surface features.

2.4 Summary and Conclusions

We have reported on a diverse set of Monte Carlo simulations of homogeneously and heterogeneously charged polymers adsorbing to various patterned surfaces. The chain entropy prevents efficient pattern recognition between the polymer and the surface. As a result, the equilibrium quantities such as adsorption energy and radii of gyration of the adsorbed polymer are dictated by the size of the surface charge blocks and their geometric correlation to the polymer charge density. Our results show that simply increasing the interactions between polymer segments and the surface pattern is not sufficient to achieve molecular pattern recognition. Perfect pattern matching in polymeric systems requires both (1) a reduction of loops favored by entropy and (2) the ability of those loops to desorb from intermediate states. This can be achieved by selecting the proper range of polymer-surface interactions. We found that long runs of one kind of polymer segment or pattern feature will, in general, enhance recognition.

The effects of correlated sequence fluctuations between the polymer and surface on pattern recognition have not been exhaustively investigated in this project. Our computer time was limited due to the large number of polymer-surface combinations we investigated. We were not able to study any one type of charged

polymer or charged pattern in a thorough manner. The final reported data from our studies were averaged over only four sets of simulation runs.

Our results show that positive/negative polymers prefer the positive/negative checkerboards, even more so than the uniform positive surface. One would intuitively expect the uniform positive surface to be less repulsive to the mixed-charge polymer. Possible extensions of our work could focus more thoroughly on these positive/negative species adsorbing to positive/negative surfaces. Detailed studies are needed of the effects of varying the sizes of charge blocks on the polymer as well as the surface. We followed the equilibrium quantities of adsorption energy per segment and the radii of gyration of the adsorbed chain. Kinetic studies could be done to follow the polymer as it interacts with the patterned surface. The position of the chain as a function of Monte Carlo time would reveal a great deal of information. This would allow us to watch the polymer rearrange as it traverses the meta-stable states and give us an idea of how long the final adsorption takes.

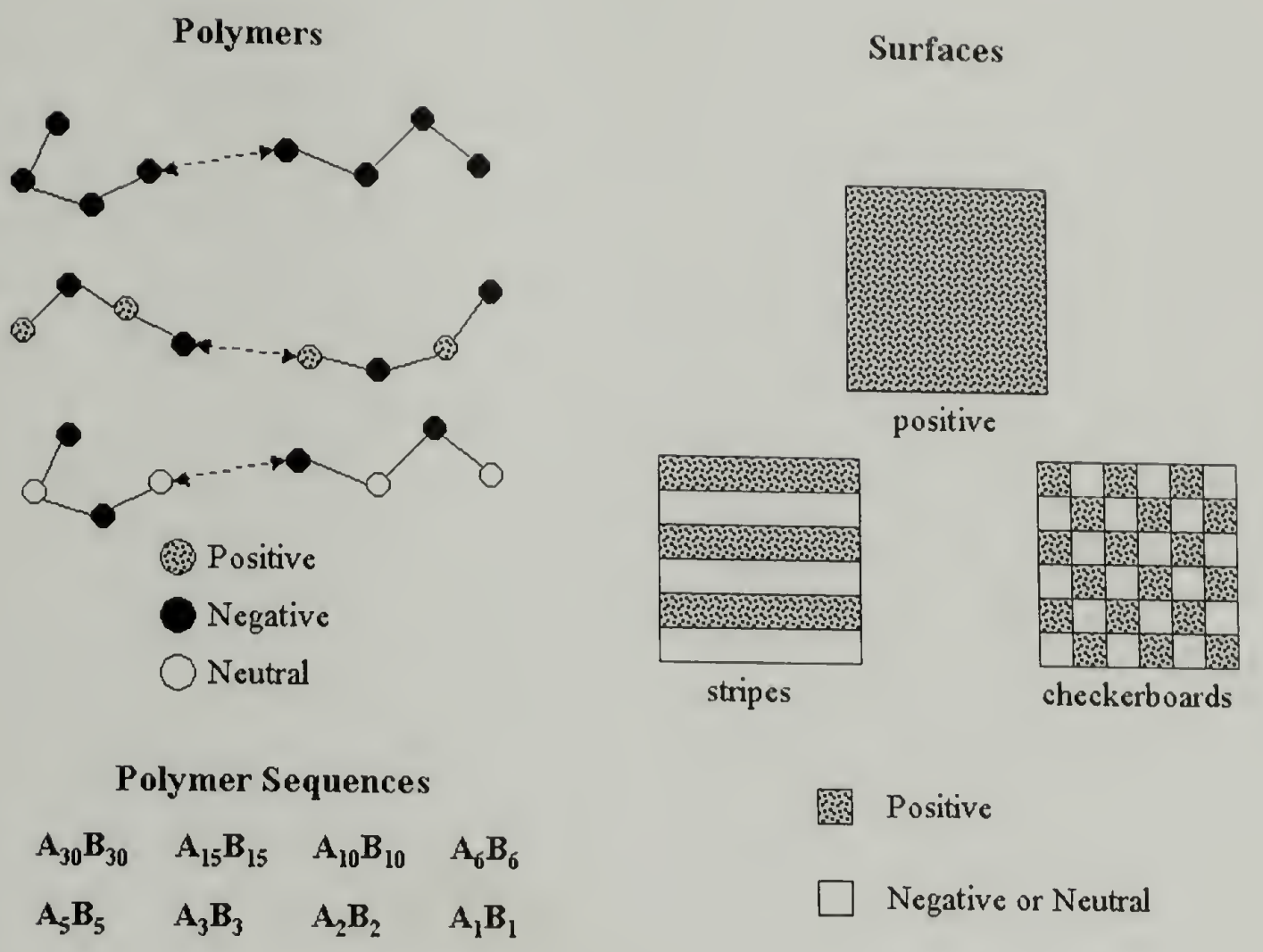

Figure 2.1. Various polymers and surfaces modeled in the simulations. Negative homopolymer of length 60, positive/negative block copolymer of length 60, and negative/neutral block copolymer of length 60. Length (x) of alternating blocks of A and B: A_XB_X. Uniform positive surface, stripes of alternating positive and negative or positive and neutral charge, and checkerboards of alternating positive and negative or positive and neutral charge.

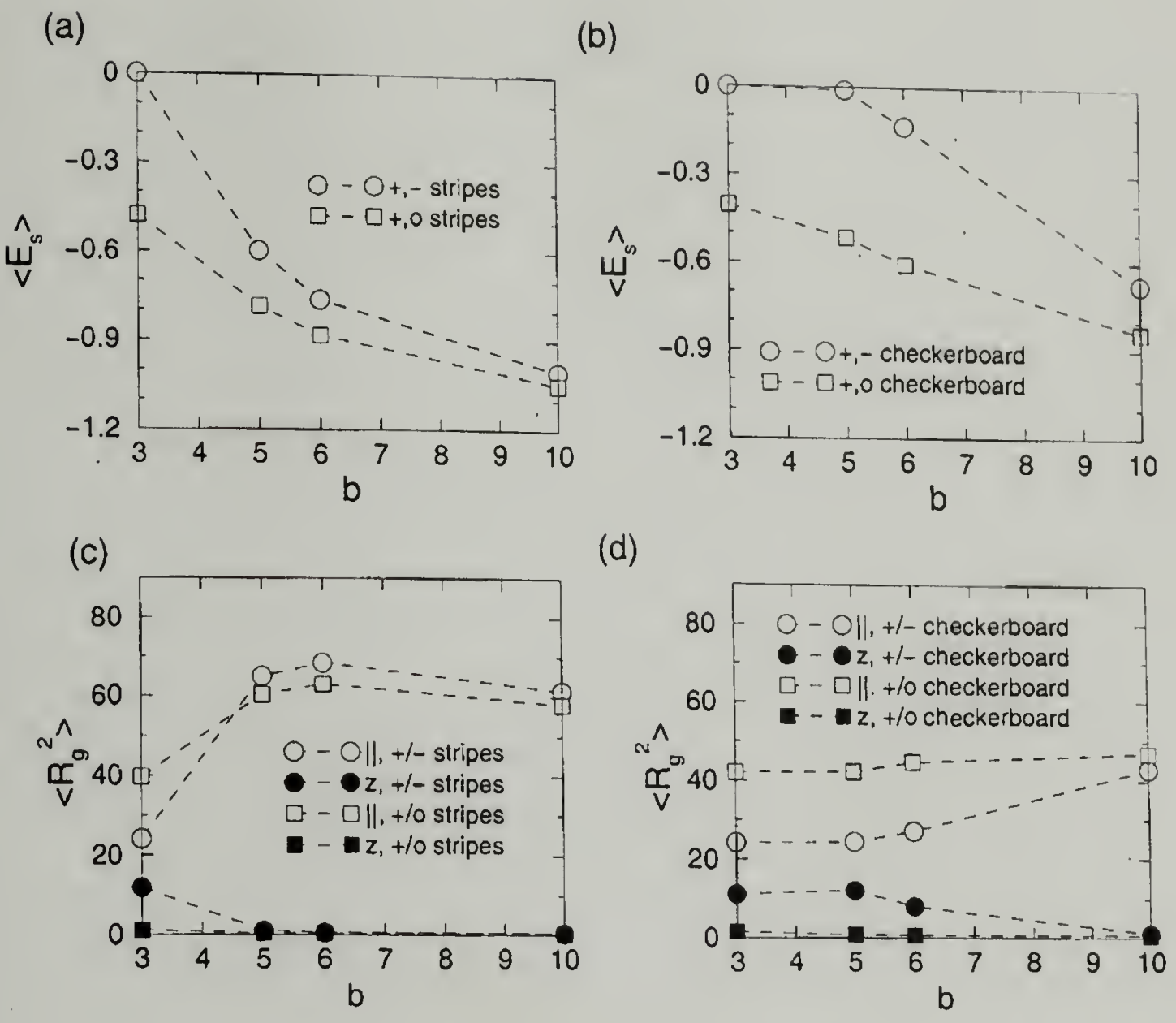

Figure 2.2. Average energy per segment and average radii of gyration squared as a function of stripe and checkerboard size with the negative homopolymer. Average absorption energy per segment for (a) striped surfaces, (b) checkerboard surfaces. Average radii of gyrations squared for (c) striped surfaces, (d) checkerboard surfaces. Open symbols: $\langle R^2(xy) \rangle$ and filled symbols: $\langle R^2(z) \rangle$

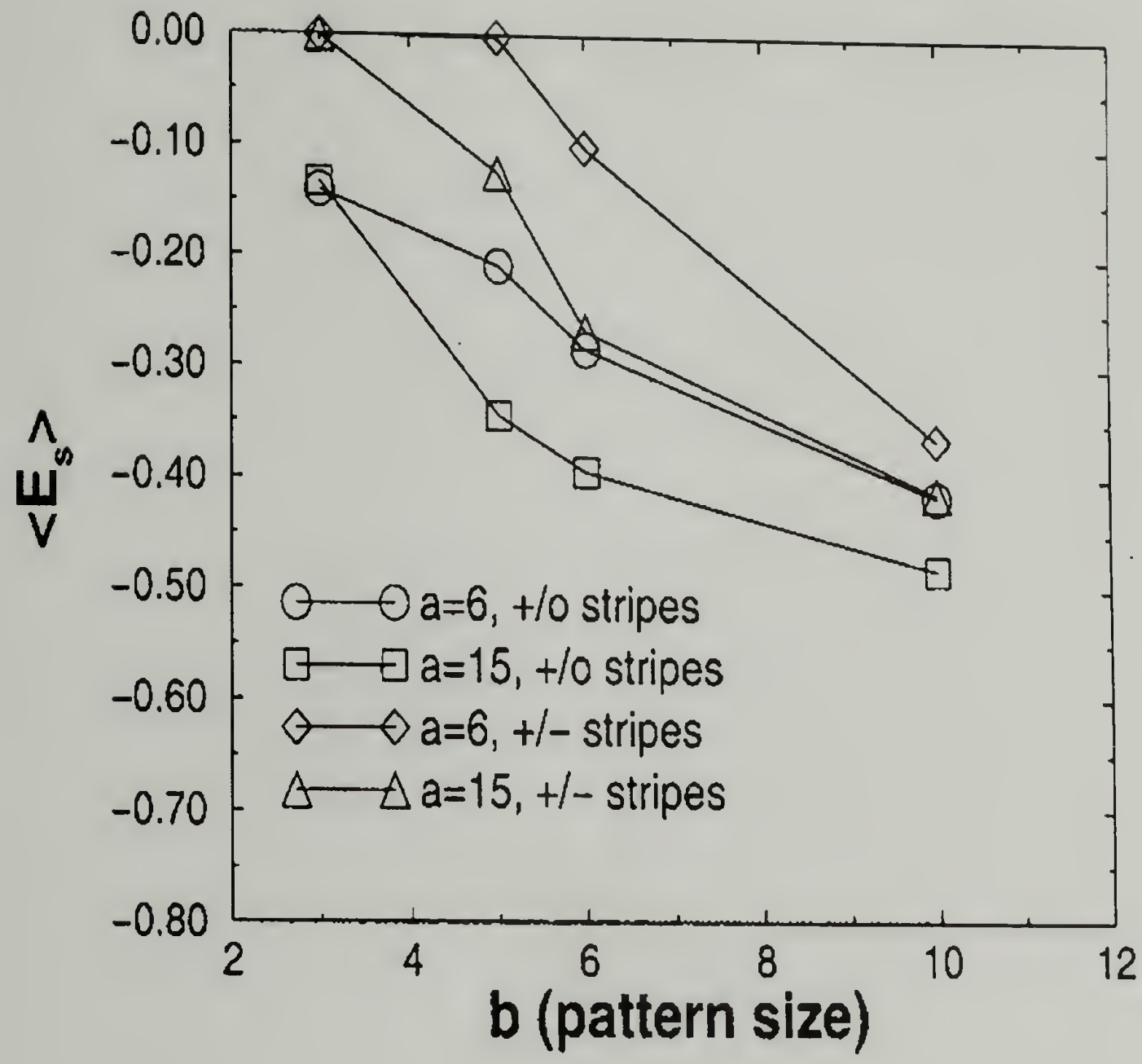

Figure 2.3 Average adsorption energy per segment as a function of stripe width. Average adsorption energy per segment for negative/neutral block copolymers on striped surface patterns. Alternating negative/neutral polymer blocks of length 6 and 15 with positive/neutral and positive/negative stripes.

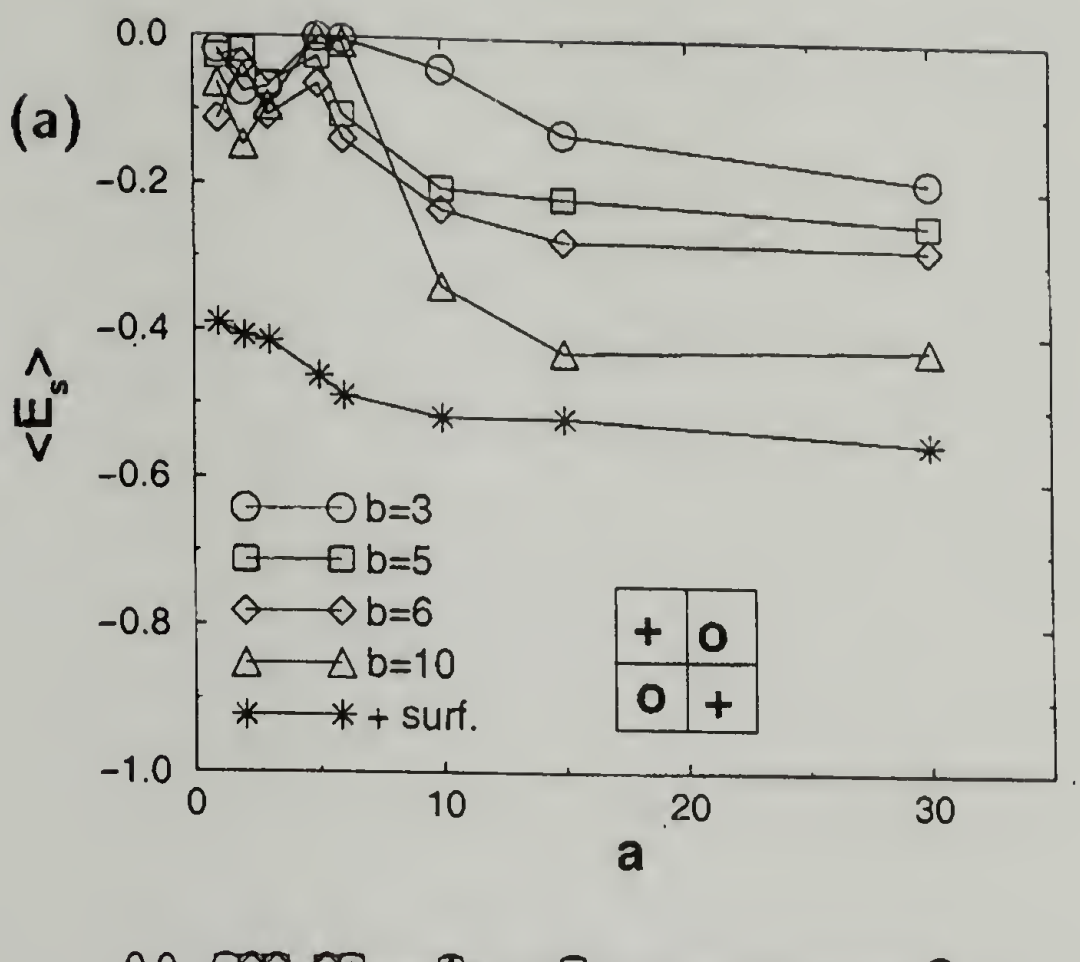

Figure 2.4 Average adsorption energy per segment as a function of negative/neutral polymer block length. Average adsorption energy per segment for negative/neutral block copolymers on checkerboard surfaces for (a) positive/neutral checkerboards of size 3, 5, 6, and 10, (b) positive/negative checkerboards of size 3, 5, 6, and 10. Uniform positive surface also simulated for comparison.

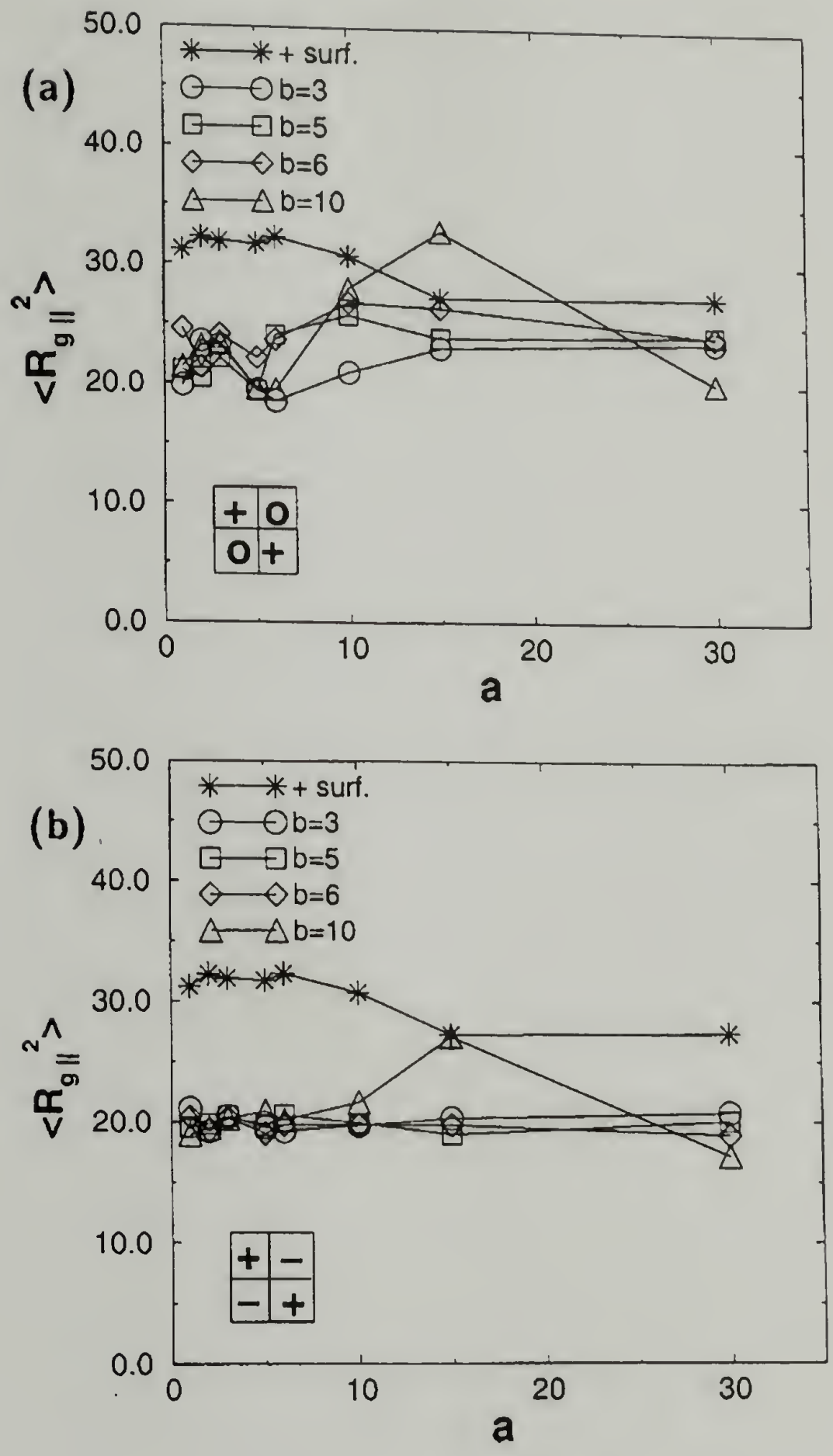

Figure 2.5. Average radii of gyration squared $<R^2(xy)>$ as a function of negative/neutral polymer block length. Average radii of gyrations squared for negative/neutral block copolymers on checkerboard surfaces for (a) positive/neutral checkerboards of size 3, 5, 6 and 10, (b) positive/negative checkerboards of size 3, 5, 6 and 10. Uniform positive surface also simulated for comparison.

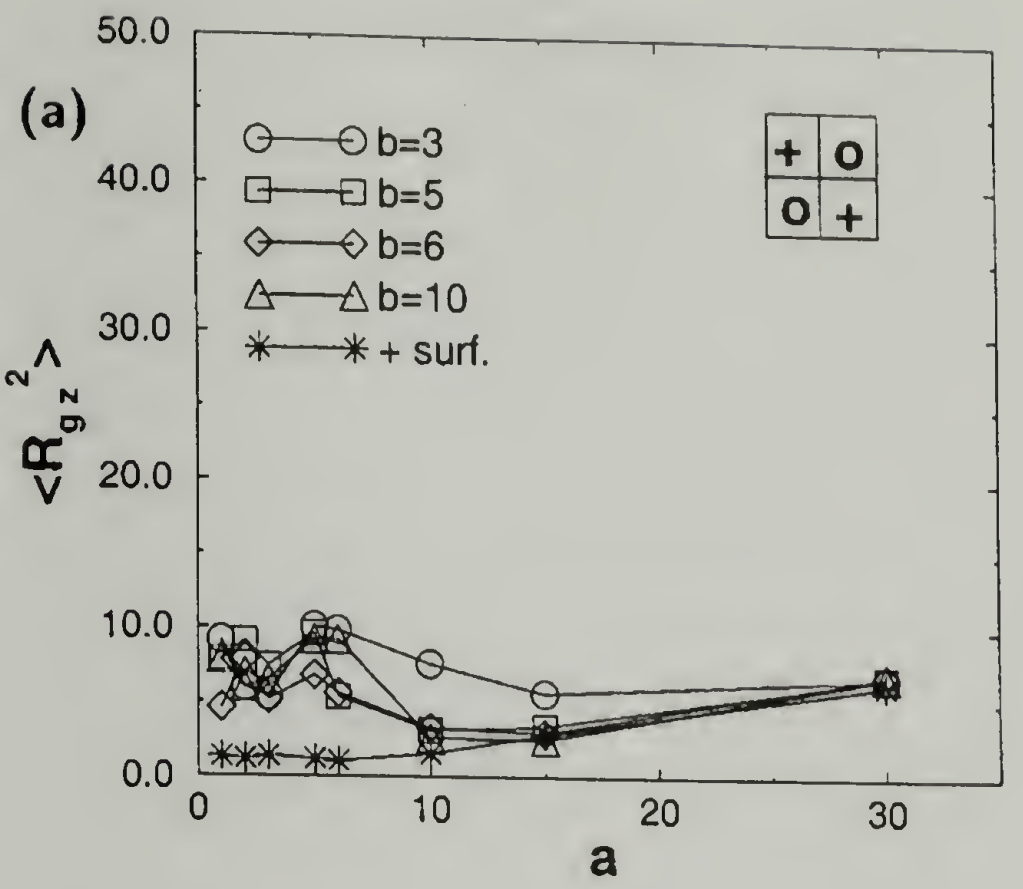

Figure 2.6. Average radii of gyration squared $<R^2(z)>$ as a function of negative/neutral polymer block length. Average radii of gyration squared for negative/neutral block copolymers on checkerboard surfaces for (a) positive/neutral checkerboards of size 3, 5, 6 and 10, (b) positive/negative checkerboards of size 3, 5, 6 and 10. Uniform positive surface also simulated for comparison.

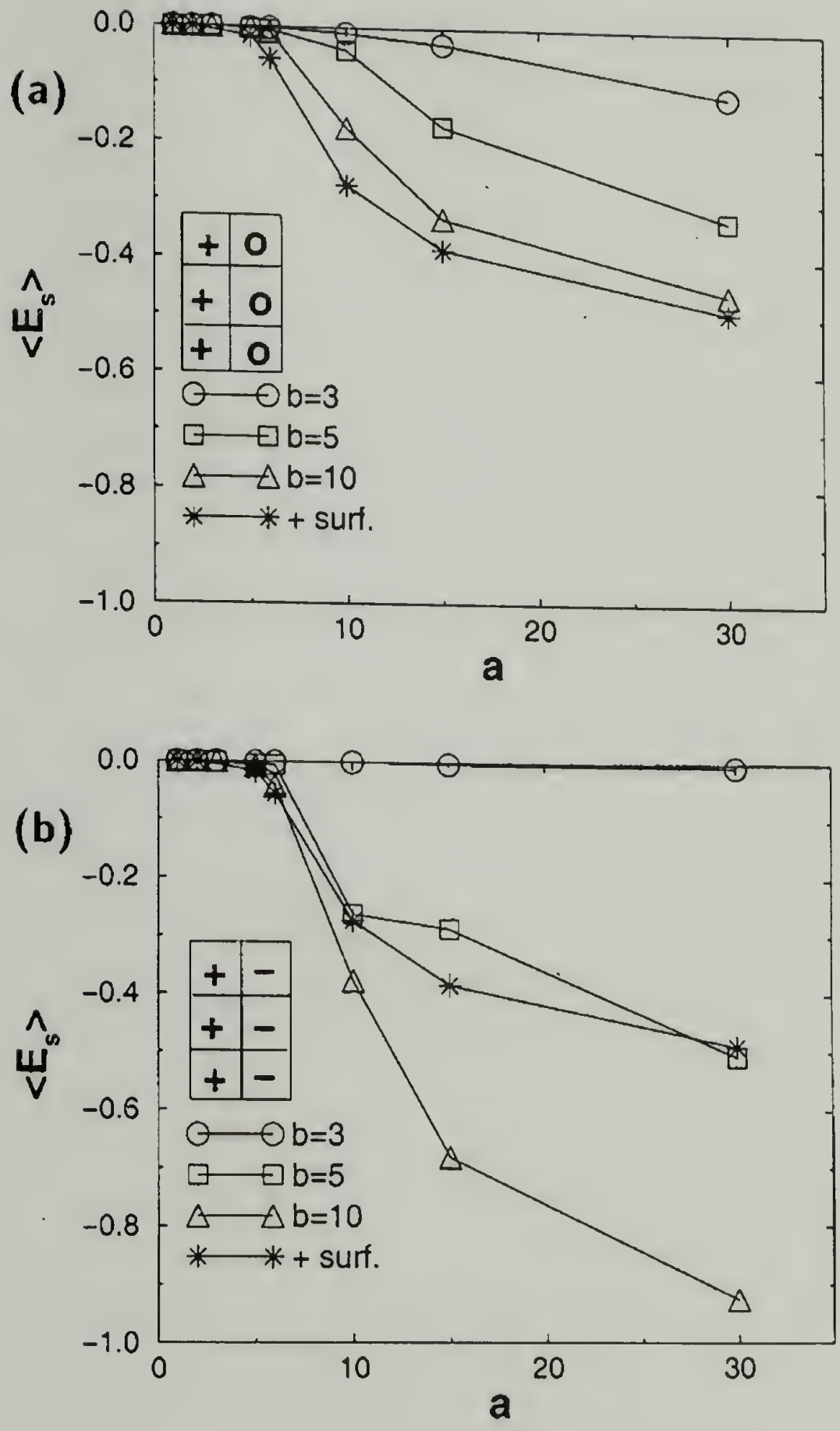

Figure 2.7. Average adsorption energy per segment as a function of positive/negative polymer block length. Average adsorption energy per segment for positive/negative block copolymers on striped surfaces for (a) positive/neutral stripes of size 3, 5 and 10, (b) positive/negative stripes of size 3, 5 and 10. Uniform positive surface also simulated for comparison.

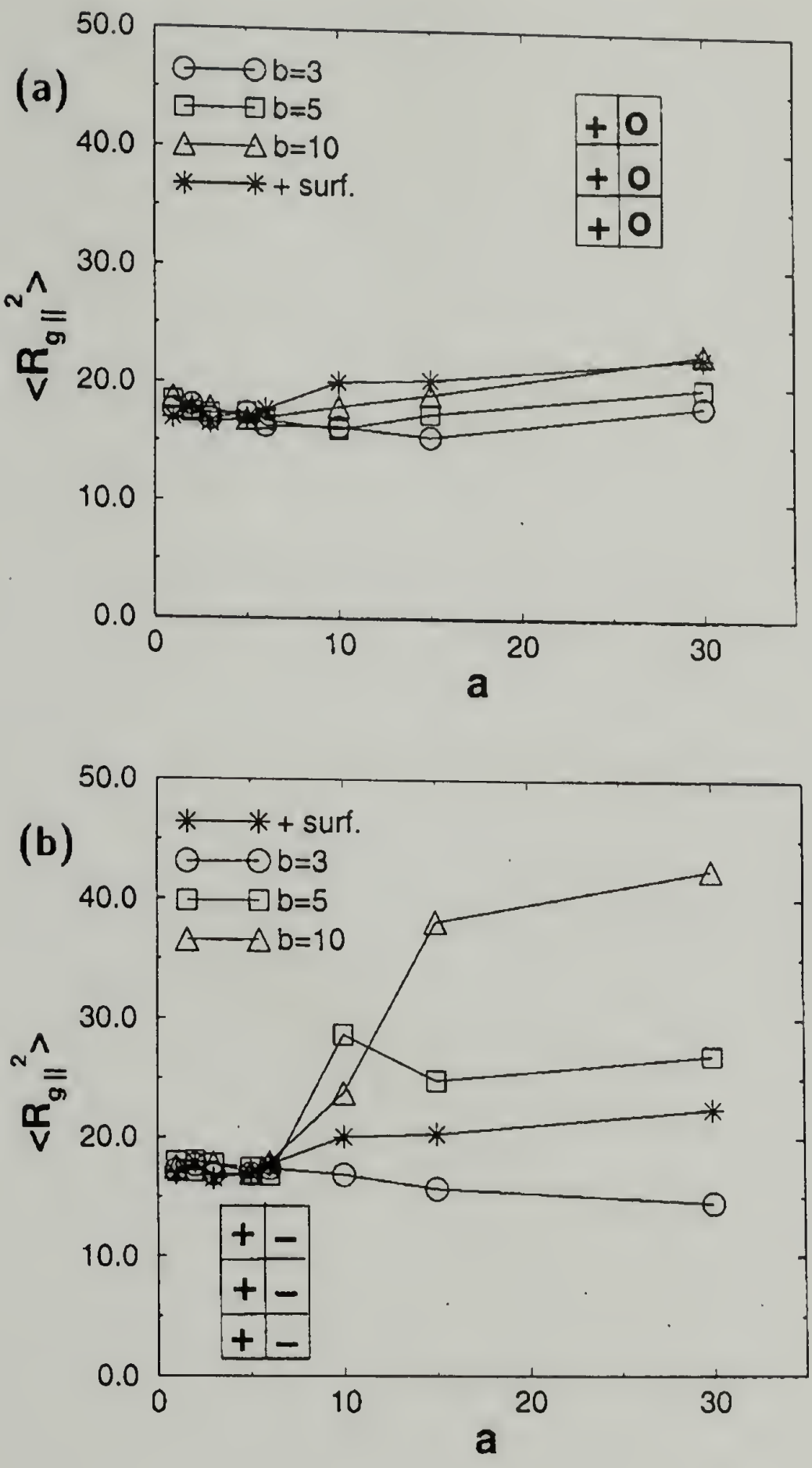

Figure 2.8. Average radii of gyration squared $<R^2(xy)>$ as a function of positive/negative polymer block length. Average radii of gyrations squared for positive/negative block copolymers on striped surfaces for (a) positive/neutral stripes of size 3, 5 and 10, (b) positive/negative stripes of size 3, 5 and 10. Uniform positive surface also simulated for comparison.

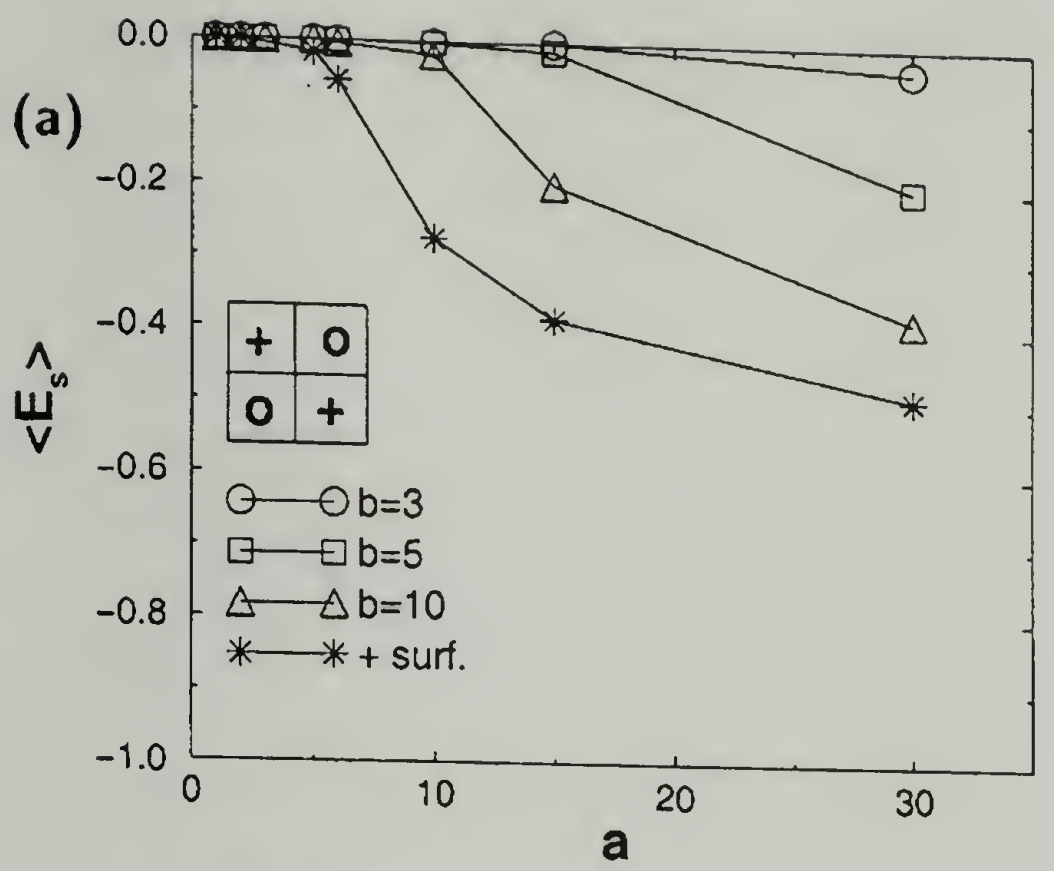

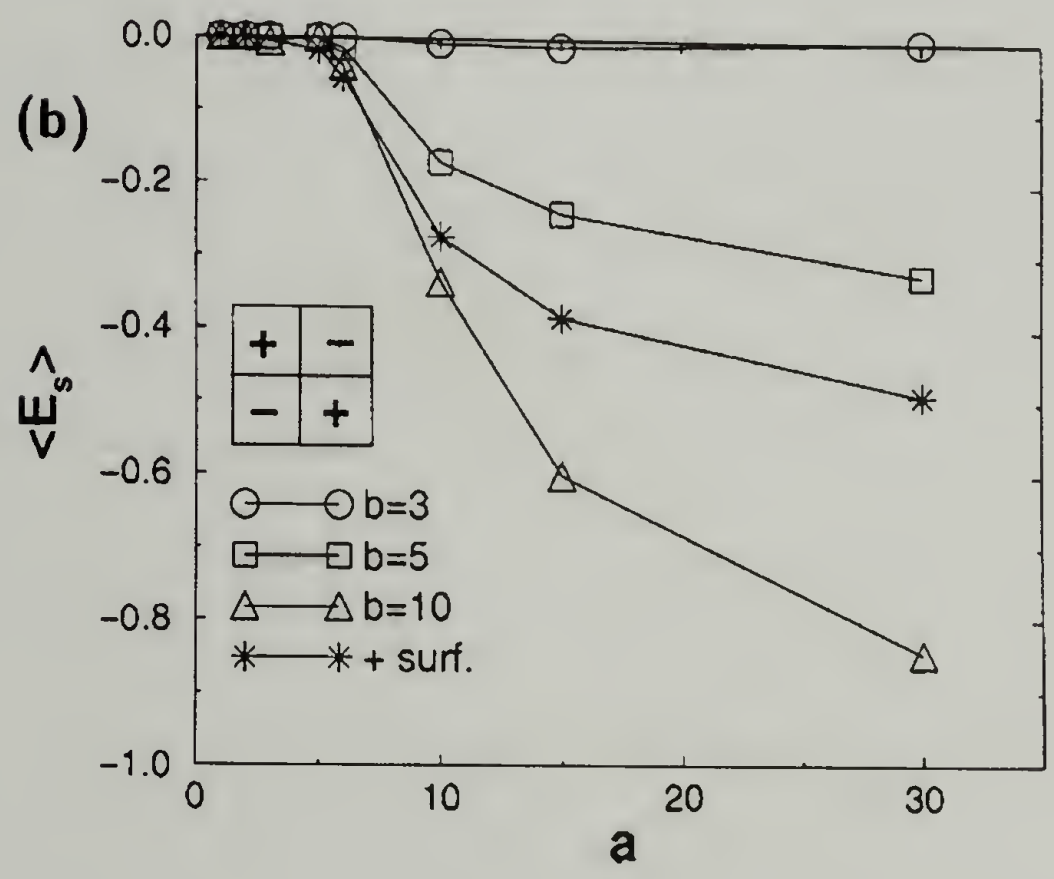

Figure 2.9. Average adsorption energy per segment as a function of positive/negative polymer block length. Average adsorption energy per segment for positive/negative block copolymers on checkerboard surfaces for (a) positive/neutral checkerboards of size 3, 5 and 10, (b) positive/negative checkerboards of size 3, 5 and 10. Uniform positive surface also simulated for comparison.

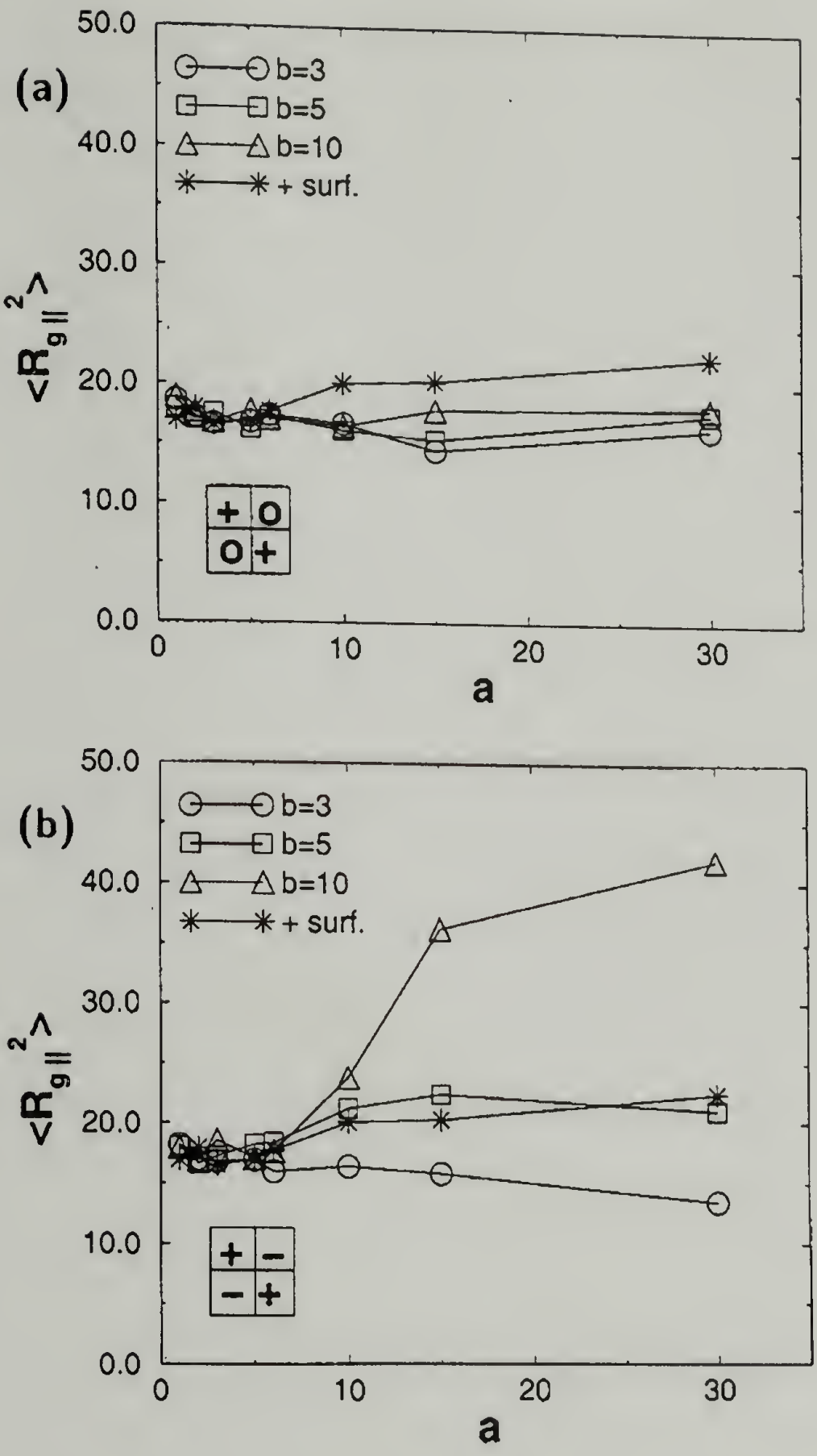

Figure 2.10. Average radii of gyration squared $<R^2(xy)>$ as a function of positive/negative polymer block length. Average radii of gyrations squared for positive/negative block copolymers on checkerboard surfaces for (a) positive/neutral checkerboards of size 3, 5 and 10, (b) positive/negative checkerboards of size 3, 5 and 10. Uniform positive surface also simulated for comparison.

CHAPTER 3

DILUTE POLYETHYLENE CRYSTALLIZATION FROM PARAXYLENE VIA SMALL ANGLE LIGHT SCATTERING

3.1 Introduction

Polyethylene (PE) is one of the most abundant and well-studied synthetic polymers known. It is produced from petroleum derivatives and its versatility and low bulk cost makes it a popular manufacturing material. Dilute-solution-grown crystals have contributed significantly to the understanding of polymer crystallization. The driving forces for the formation of single crystals in dilute solution are the same as in bulk, but single crystals lack the more complex bulk morphologies [25,26]. Linkages between crystals and aggregates are more probable as polymer concentration increases. One drawback of dilute-solution-grown crystals is that their small sizes most often require transmission electron microscopy (TEM) or specialized optical-microscopy techniques for visualization. Single crystals generally are thin 10nm platelets that are on the order of 1 micron wide in the temperature and concentration regimes normally studied.

Kinetic studies of dilute-solution-grown PE crystals have been well documented [27-29]. The growth rates of single crystals are usually calculated from electron micrographs of frozen crystals. Most of these studies have been done in the 0.01 to 0.1 wt.% concentration regimes. Freezing the crystal allows the growth to be stopped and structure preserved at fixed time intervals. These rates have been tabulated for various organic solvents [30], as have the effects of polymer concentration [31,32] and molecular weight [33] on the rate of crystallization. An

order of magnitude increase in growth rate of single crystals in xylene is observed with only a 5°C drop in crystallization temperature. Also, the concentration dependence on growth rates scales as $G \propto C^{\alpha}$, where α is a constant and increases with temperature. For sufficiently low polydispersity PE in xylene, quenched below 86°C, α is between 0.40 and 0.80 [27]. A. Keller and E. Pedemonte [27] studied PE (2,600 g/mole, 1.5 polydispersity) crystallization from xylene in the 0.01 to 0.1 wt.% regimes. For a 80.0°C quench, the growth rate of a 0.1 wt.% solution was 3 μm/hr. And for a 74.9°C quench, the growth rate of a 0.1 wt.% solution was 30 μm/hr. Others report similar results for PE crystallizing from organic solvent [28-29].

A typical single crystal is 10 nm thick in the fold direction and a few microns, at most, in the lateral direction as in Fig. 3.1(b). Crystals grown with the self-seeding technique are generally larger and more uniform in size [34,35]. The morphology of PE single crystals depends strongly on the crystallization temperature and on the polymer concentration (See Fig. 3.1(a)). The thickness of the chain folding in PE never varies more than ±10%. The crystals nucleate from a central point outward in a [110] or [100] direction as they chain fold. Polymers form stacks of these folded chains in the growth plane called lamella. As the chains fold and more polymers add to the crystal, the polymer increases its size in the lateral direction. Picture a small piece of cardboard getting larger, with its thickness remaining constant. The shape of these flat platelets can range from irregular dendrites with rough edges [36], to uniform diamonds, to truncated diamonds and smooth lozenges [37,38]. These transitions from dendrites to lozenges are a function of increasing quench temperature. Also, decreasing concentration has a similar effect.

Although electron microscopy is the tool of choice in PE kinetic crystallization studies, it cannot be used until the crystals are removed from solution. Small Angle Light Scattering (SALS) can be used to monitor crystal growth *in situ* and probe the micron-scale structures [39,40]. The integrated SALS data provides information about the growth of crystals in both their size and number. An increase in intensity corresponds to growing number of crystals and a shift in the intensity peak is related to a change of structural size.

Using SALS, we study the time evolution of scattering of dilute PE in *para*-xylene for several different crystallization temperatures. As far as we know, this is the first time SALS has been used to study dilute PE crystallization from organic solvent. We were able to measure scattering for multiple quench depths using two different linear-low-polydispersity PE samples in *para*-xylene. We find asymmetric oval scattering for 0.05 wt.% PE solutions quenched below 70-75°C and symmetric scattering above those temperatures. In addition, we find asymmetric oval scattering for 0.1 wt.% PE solutions quenched below 70-75°C and symmetric scattering above those temperatures. The transition is smooth with temperature and possibly a few degrees higher for the 0.1 wt.% PE solutions. All results were reproduced for both PE samples. From the scattering data as well as the results of TEM we performed, we conclude that the differences in scattering may be due to ordered assemblies of single crystals.

This chapter is organized as follows: the methods and materials are explained in Sec. 2; our results are given in Sec. 3; the conclusions are summarized in Sec. 4.

3.2 Small Angle Light Scattering

Wave scattering, in general, is due to patterns of interference of propagating waves by planes of scattering centers within the sample. SALS techniques are useful in probing structures from a few microns to a few hundred microns. The scattering angle is the angle between the incident direction of the light and the scattered direction. Large structures scatter at small angles, while smaller structures scatter at larger angles. The specific angles can be calculated from Bragg's law:

$$n\lambda = 2d\sin\theta \tag{3.2.1}$$

where n is the order of diffraction, λ is the incident wavelength, d is the distance between scattering planes and θ is the Bragg angle which is one-half of the physical scattering angle. The scattering vector $\boldsymbol{q}$ is the vector difference between the wave propagation vectors of the incident and scattered beam and has units of inverse distance. This vector is in the plane of the scattering pattern and points from the incident beam to the scattered beam. The magnitude of $\boldsymbol{q}$ that corresponds to the maximum scattering intensity q_{max} is related to d through the equation:

$$d = 2\pi / q_{max} \,. \tag{3.2.2}$$

We have built a SALS instrument that can take scattering pictures at fixed time intervals and is fully automated (See Fig. 3.2). Our new system is made up of a 10mW Helium-Neon laser from Uniphase, Newport as well as Oriel rotating polarizers (1/2λ wave plates), a Panasonic 1/3 inch WV-BP330 RS-170 type CCD camera, a Computar 8mm manual focus F1.2 lens, a homemade aluminum sample holder connected to a NesLab RTE-111 water circulator, a homemade screen for the SALS image and a 50.0 mm^2 unbiased silicon photo-diode with a BNC mount from

Edmund Optics, all wall-mounted on vertical steel track. The sample holder has channels within it that circulate a water/ethylene glycol mixture to maintain the temperature within ±0.5°C. The maximum temperature of our water/ethylene-glycol circulator is 95-100°C. The sample holder and screen rest on stages with clamps that can be manually moved along the vertical track.

We purchased quartz light scattering cells from Hellma & Co. These QS-120 cells have a 2-millimeter optical path length and fit snuggly inside our aluminum sample holders. We also purchased Pyrex light scattering cells of the same dimensions from Starna Cells, Inc. The screen is covered with linear polarizing film from Edmund Optics with a small hole in the center so the transmitted beam can be measured for intensity with the photo-diode. The film acts as a SALS analyzer lens, which can be rotated. The camera is offset at angle above the SALS screen on a smaller vertical track with clamps that can also be manually moved up or down as well as rotated. The Dell Optiplex GX270 computer that records the images and analyzes the data is controlled via a custom program written in LabVIEW 7.0 with IMAQ Vision 7.0. It is interfaced with a NI PCI-6013 A/D board for the photo-diode signal and an NI IMAQ PCI-1407 image board for a standard RS-170 type CCD camera.

The SALS control panel can record any number of images at fixed time intervals of five or more seconds. It takes about five seconds to do corrections for camera and screen geometry and then process the data. The images are corrected for camera angle and screen tilt with a uniform grid of black circles and a short calibration program as outlined in the LabVIEW manual. A photo is taken of the distorted circles and a matrix is created to translate and rotate the images. The

distance from the sample to the screen is entered via the main program and used to calculate the q-values. A diffraction grating is not needed to calibrate our SALS system. Nevertheless, when we used a 100 line per millimeter grating our q-values were within 1% for the first order peaks. The scattering images are taken with a monochrome camera. A RGB color scheme is used to highlight intensity differences that are set with a 0 to 255 scale. Red is for the highest intensities, followed by orange, then yellow, then green and finally blue for the background.

The range of sample-to-screen distances is 25 to 150 cm, which corresponds to a q-range from 0.033 to 3.00 μm^{-1} and a d-spacing from 190 to 2.09 μm, respectively. All of our data are for a 45.0 cm sample-to-screen distance. At this distance, we can probe structures from 45 down to about 3 μm.

3.3 Sample Preparation and SALS Procedure

Linear PE with low polydispersity was chosen to minimize defects and provide more ideal single crystals. Rajeswari Kasi of the E. B. Coughlin research group at the Polymer Science and Engineering Department, University of Massachusetts, Amherst synthesized the first PE sample we used. This linear PE was synthesized from an ethylene monomer using a homogeneous-constrained-geometry catalyst (DOW-INSITE) with an MAO co-catalyst at room temperature. It had a polydispersity of about 1.6 to 1.8 and melting point of 135°C and was at least 60% crystalline. This sample of PE had a weight-averaged molecular weight of around 200,000 g/mole. The second sample of linear PE was purchased from NIST and had a weight-averaged molecular weight of 119,600 g/mole and polydispersity of only 1.19.

We purchased two lots of 0.3 grams each. While we report results for both PE samples, we only present data for the higher quality NIST sample.

We used 99+% HPLC grade *para*-xylene purchased from Fisher Scientific as the solvent in our experiments. This solvent was chosen for its lower dissolution and crystallization temperatures. The solvent has a molecular weight of 106.17 g/mole and a density of 0.8611 g/mL. The *para*-xylene was filtered through a 0.45 μm PTFE filter into 50 mL clean glass laboratory jars with a PTFE cap that screwed on. The dissolution temperature of linear PE in *para*-xylene is about 115°C.

The samples prepared for SALS contained 0.05 wt.% or 0.1 wt.% of PE in the *para*-xylene. We added 0.0086 grams of linear PE to 20 mL of solvent to create the 0.05 wt.% solutions. Also, 0.0086 grams of linear polyethylene was added to 10 mL of solvent to create the 0.1 wt.% solutions. Batches of the 10 mL or 20 mL stock solution were prepared and then used for 2-3 weeks. Although the solutions were very dilute, single crystals were produced with a measurable scattering as well as a decrease in main beam transmission.

The capped 50 mL jar of stock solution was heated and stirred with a magnetic stir bar for 30-60 minutes at about 120°C to dissolve all of the PE. Subsequent dissolutions of the same stock solution required less time. Care was taken not to approach the 138.3°C boiling point of *para*-xylene. Samples were then transferred via a clean 1.0 mL glass syringe with disposable needle to a 560 μL cylindrical quartz light scattering cell. The cells were then heated again to about 120°C to re-dissolve the PE. We used two aluminum sample holders to reduce the transfer time to the SALS. The sample holder for SALS was set at the crystallization temperature (from

60°C to 85°C). The other holder rested on a heating plate (set at 118-120°C) and was located next to the SALS apparatus. The light scattering cells were heated on the hot plate for about 30-40 minutes and then quickly transferred to the SALS instrument. It took about 15 seconds to transfer the solutions and start the SALS program.

Once the program was started, depending on the quench depth, initial scattering was seen between 1 and 20 minutes. For every scattering image, the transmitted intensity was measured and scattering intensities integrated and plotted versus the q-values along the 270° lines of the scattering patterns. For symmetric scattering, the intensity versus q-values will be independent of the chosen line.

The laser light was polarized horizontally to the scattering patterns for all of our SALS studies. All of our analysis was for the analyzer in the same direction relative to the initial polarization. This is called vertical-vertical (V_V) scattering. Our studies show very little anisotropy in our dilute polymer solutions, thus there is no noticeable horizontal-vertical (H_V) scattering.

The transmission of the main beam through the sample, the intensities versus q-values, and the temperatures were saved in Excel files. There was one data set for every scattering picture taken. All scattering patterns were saved as binary image files (.png) of size 728 × 527 pixels. The intensities saturated if their values were above 255. In that case, the camera iris could be closed to decrease its sensitivity to the laser light. The pixel coordinates of the center of the images as well as the q-values were saved in a separate text file for further data analysis.

A cleaning regimen was established to ensure that our samples were free of contaminants and that the light scattering cells had no residue on the interior. The

glass jars and the glass syringe were cleaned with a low-residue cleaning solution of 2% Micro90 from Cole-Parmer in purified RO water. The Pyrex and quartz cells were cleaned with the recommendations of Starna Cells, Inc. This included initial rinses with hot (about 118-120°C) filtered *para*-xylene, a warm (60-70°C) rinse of 2% Micro90 in purified RO water, a strong acid (1N HCl) wash, followed by several rinses of purified RO water. This regimen worked well except when the PE solution remained in the cells for several days. A mixture of NOCHROMIX (Godax Laboratories) with concentrated sulfuric acid (0.35g/5mL) was used for aggressive cleaning. The quartz cells were cleaned in the initial experiments with 2% Hellmanex II (Hellma & Co.) in purified RO water. This is a basic surfactant/detergent cleaner that did not work as well as the Starna recommendations. Cells were cleaned between all SALS experiments.

3.4 Small Angle Light Scattering Results

3.4.1 PE Synthesized In-house

0.05 wt.% solutions of the 200,000-g/mole PE were initially quenched to 65°C and 80°C and measurements were made for 2 to 3 hours at 30-second intervals. After analyzing the scattering for the 65°C quench, we found oval patterns perpendicular to the laser polarization. When we changed the polarization direction, the scattering patterns rotated perpendicular to that new direction. The scattering for the 80°C quench produced symmetric patterns. The values of the Bragg spacings ($d=2\pi/q_{max}$) were about 15 μm for both temperatures. The onset of scattering for 65°C quench was

on the order of 1 to 1.5 minutes. For the 80°C quench, the onset of scattering was about 4 to 4.5 minutes. After the initial drop, there was little change in transmission for both temperatures.

The dramatic difference in scattering for these two quenches could not be explained in terms of early-stage crystallization. Data from previous TEM studies of single crystal growth rates show little difference in single crystal morphology. For the 70-80°C quenches, the single crystals are usually diamond shaped with [110] facets only. The lower 65°C quenches usually produce the same faceted structures with rougher edges [12]. In both cases, the crystals are about 10 nm thick in the fold direction and micron size in the lateral growth direction. Why the scattering was symmetric for the higher temperature quenches, but asymmetric for the lower temperature quenches needed to be answered.

We made several more samples and SALS was repeated with the same results. We then checked if our dilute PE solutions were in equilibrium after quenching. After a 65°C quench producing the oval scattering patterns, we heated the cell back up to 120°C to re-dissolve the crystals. The 80°C quench was then done to check for hysteresis. The results showed the same symmetric scattering with no history dependence. The cell was then heated again and quenched to the lower temperature producing the oval scattering patterns.

The possibility of thermotropic transitions in the scattering was investigated. The 65°C quench was allowed to equilibrate for several hours and then the PE solution was cooled to room temperature with no changes in the scattering. The 80°C quench was equilibrated for several hours and then the temperature was reduced to

65°C. The scattering likewise did not change. It was concluded that the observed scattering was not due to non-equilibrium phenomena or thermotropic ordering.

The scattering of the solvent alone as well as that of the empty cell was checked for contribution to the overall scattering. There was little contribution to scattering for both temperatures investigated, 65°C and 80°C. Also, since the background scattering was subtracted from all the SALS runs, this was not a major concern.

The possibility of surface interactions of PE crystals with the quartz was also investigated. Two of the quartz cells were treated with a hydrophobic silanating agent and non-quartz Pyrex cells were used as well. Sung In Moon of the T. McCarthy research group at the Polymer Science and Engineering Department, University of Massachusetts Amherst did the silanation. This procedure ensured that the cell interior was not hydrophilic due to the cleaning process and causing surface ordering. The same results were obtained with the silanated quartz cells and the Pyrex cells. It was clear that the scattering was not due to surface adsorption or surface-induced ordering. The next step was to check these results with another sample of linear PE. We needed to be certain that our results were not unique to the PE sample we used.

3.4.2 NIST PE 0.05 wt.%

We used the NIST sample to reproduce the scattering results. The 0.05 wt.% solutions were initially quenched to 65°C and 80°C and measurements were made for 2 to 3 hours at 30-second intervals. The results were identical to the previous results for both quenches. For the 65°C quench, we found the oval patterns perpendicular to

the laser polarization as in Fig. 3.3. The onset of scattering was also about 1 to 1.5 minutes after the quench. The scattering for the 80°C quench produced symmetric patterns as in Fig. 3.4. The onset of scattering was again about 4 to 4.5 minutes after the quench. Transmission data for these quenches showed that the beam intensity decreased in about 2 to 2.5 minutes for both temperatures. See Figs. 3.5 and 3.6 for the transmission of the main beam versus time. There was little change in transmission data after the initial drop in intensity in both cases.

The effects of non-equilibrium phenomena, thermotropic ordering, background scattering and surface interactions were also investigated for the NIST sample at 0.05 wt.% and shown to be negligable.

We hypothesized a rod-like morphology for the 65°C quenched crystals since they could then self-assemble into a nematic phase and produce the asymmetric scattering patterns. The 80°C quenched crystals were thought to be more like the conventional [110] faceted diamond shaped platelets, randomly tumbling in solution with no net orientation. We attempted to look at the crystals in solution obtained for 65°C and 80°C quenches with optical microscopy to determine their morphology. The results of several optical microscopy techniques did not reveal any data for the crystals due to lack of contrast between the solvent and crystals and the small size of the crystals. SAXS was attempted but was not successful due to too little scattering from these dilute solutions. Therefore no data are shown for these techniques. Subsequently, we used TEM with carbon-coated copper grids to examine the crystals after evaporation of the *para*-xylene.

The crystals were equilibrated overnight at the quench temperatures and then one to three drops of solution were placed on the TEM grids. The overnight equilibration was done to ensure all dissolved PE had crystallized. (Note that it is possible for the crystal structure to change as the solvent evaporates on the grid because it increases the concentration of polymer.) The TEM used was a 100keV JEOL 100CX system. Imaging was performed with the help of Lou Raboin of the Polymer Science and Engineering Department, University of Massachusetts Amherst.

We determined the crystals quenched at 65°C were not rod-like and were in fact the rough-edged diamond platelets that most studies had reported. Their size was on the order 0.25 to 0.5 μm in the lateral direction shown in Fig. 3.7. The crystals quenched at 80°C were more regular-shaped diamond platelets on the order of 0.75 to 1.0 μm as in Fig. 3.8. The number of crystals for the 65°C quench was higher than for the 80°C quench. This is reasonable since the deeper quench should produce more nucleating sites. Also, the crystals should be larger for the 80°C quench since there are fewer of them nucleating farther apart. In any case, it was clear that the difference in scattering that we had seen was not due to early-stage crystal growth kinetics.

We further tested the possibility of liquid-crystalline ordering by performing quenches to 60°C, 70°C, 75°C, and 85°C to see if the crossover was smooth or sudden. The 60°C quench produced the same oval scattering seen in Fig. 3.9 with the onset of scattering a little sooner than in the 65°C quench. The q_{max} increased with time as with the other quenches indicating decreasing correlation size. The crossover was smooth and occurred between 70 and 75°C as in Figs. 3.10 and 3.11. For the

85°C quench, the scattering was very symmetric with the onset of scattering at about 10 minutes as seen in Fig. 3.12.

This provides good evidence that we were not looking at single crystals with SALS, but at assemblies of crystals on the order of 15 to 30 μm, corresponding to the scattering peaks. In the deeper quenches, it is possible that the crystals stack and in the shallower quenches the crystals tumble with no overall orientation. The evidence for this is based on the scattering patterns, the *d*-spacing corresponding to the scattering, the turbidity data, the morphology of the crystals from TEM and the fact that crystals nucleate closer together in the deeper quenches and grow faster.

3.4.3 NIST PE 0.1 wt.%

If this was indeed a liquid-crystalline phenomenon due to the quench temperature, then it should be seen with a more concentrated solution, although the transition may occur at a different temperature.

We repeated all of the previous SALS experiments with more concentrated solutions of 0.1 wt.% PE for quenches to 60°C, 65°C, 70°C, 75°C, 80°C, and 85°C. The results for the 65°C quench showed the oval scattering perpendicular to the polarization directions. The onset of scattering was about the same as for the 0.05 wt.% solutions as shown in Fig. 3.13. The drop in transmission of the main beam occurred at 3 minutes as in Fig. 3.14. The transition temperature from asymmetric to symmetric scattering was similar to the less concentrated PE solution, and occurred between quenches to 70°C and 75°C. It is possible that the transition temperature was a few degrees higher than for the 0.05 wt.% PE solutions. Since, we only performed

SALS in 5°C increments it is not possible to verify this. The scattering patterns for the 0.05 wt.% PE solutions at the 75°C quench were more circular than the scattering patterns for the 0.1 wt.% PE solution at that quench.

The results for the 80°C quench were similar to the 80°C quench for the 0.05 wt.% solution. The only major difference was the smaller q_{max} values for the 0.1 wt.% solutions as seen in Fig. 3.15. Also, the drop in transmission of the main beam took slightly longer as shown in Fig. 3.16. All of the q_{max} values corresponded to d-spacing between 15 and 30 μm. These values are 60 to 120 times the size of the smallest crystals and 15 to 30 times the size of the largest crystals as determined from TEM. It is therefore ordering due to assemblies of crystals that we are reporting with these SALS studies and not ordering within a single crystal.

The lower temperature quenches are clearly asymmetric and show a preferred direction of scattering. This direction is always perpendicular to the laser polarization orientation. The higher temperature quenches always show symmetric scattering that one would expect from isolated single crystals in dilute solution without packing constraints. It is likely that some kind of ordering results in the lower temperature quenches. TEM studies of the crystals formed from the deeper quenches indicate that the crystals look similar in morphology to the crystal formed in the isotropic solutions.

There are two possibilities, local discotic regions of assembled single crystal platelets or large sheets of partially stacked single crystal platelets. The former would have two correlation lengths; one for the distance between aligned platelets and one for the length of the discotic region. The later would have three correlation lengths;

one for the distance between partially stacked platelets, one for the length of the large sheets of platelets and one for the distance between large sheets of platelets. The first correlation length for both possibilities may not be measurable with SALS, but the others should be micron-sized and visible with SALS.

3.5 Summary and Conclusions

We have reported kinetic studies of single polyethylene crystal formation from dilute solution of very low polydispersity PE in organic solvent using SALS. We performed multiple experiments varying quench depth and concentration for two separate samples of PE. For both samples, we found asymmetric scattering for lower temperature quenches below 70°C and symmetric scattering for the higher temperature quenches above 75°C. The transition was smooth and between 70 and 75°C for the 0.05 wt.% solutions and the 0.1 wt.% solutions. It is clear that the polymer concentration dependence is not as significant as the quench temperature on the growth rate of single crystals [27]. The correlation lengths corresponding to $d=2\pi/q_{max}$ were between 15 and 30 μm for all SALS experiments. We repeated these experiments several times with different concentrations of polymer and found the results were reproducible on our SALS system.

Our results may indicate assembled regions of single crystal platelets at lower quench temperatures below those of most TEM studies of single crystal growth rates as shown in Fig 3.17(a). Also large sheets of partially stacked crystal platelets could be forming a liquid-crystalline phase at the lower quench temperatures. These sheets would be several microns in length and as thin as 2 or 3 platelets. These sheets could

self-assemble into layers due to their high aspeet ratio. Most of the tabulated data for growth rates of PE single erystals in *para*-xylene are for quenches above 75 or 80°C; polymer eoneentrations in the 0.01-0.1 wt.% regime were also used for these studies.

For 0.05 wt.% solution of linear PE in *para*-xylene, we found possible liquid-erystalline ordering for quenehes below 70-75°C. For the eoneentration of 0.1 wt.% linear PE in *para*-xylene, we found the same ordering for quenehes below 70-75°C. The erossover to the symmetrie seattering is gradual and more SALS experiments are needed to pinpoint the exaet transition temperatures. In these symmetrie solutions, the ordering eould be the length seale at whieh the motion of erystals is eoupled or the average distanee between erystals as in Fig. 3.17(b).

Our SALS studies were only able to probe mieron-seale struetures due to the limitations of light seattering. The seattering we reported eorresponded to struetures between 15 and 30 μm. Other tools are required to eonelude that regions of staeked or aligned platelets are responsible for the asymmetrie seattering reported. The staeking of platelets can produee an ordering of about 10 nm or the erystal thiekness. SANS is a possible tool to probe 10 nm ordering and should be eonsidered to verify the sub-mieron staeking or aligning for the deeper quenehes. If large sheets of single erystal platelets formed, we would expect three eorrelation lengths, two of whieh should be measurable with SALS. Also, one would think that large 15 to 30 μm sheets of partially staeked platelets would be visible with optieal mieroseopy.

We believe that the liquid-erystalline phases observed are loeal diseotie regions due to the disk-like strueture of the erystals nueleating in elose proximity. The ordering is lyotropie and stable with respeet to temperature. When they are nueleating

farther apart as in the higher temperature quenches, they are not geometrically constrained and are able to randomly tumble in solution.

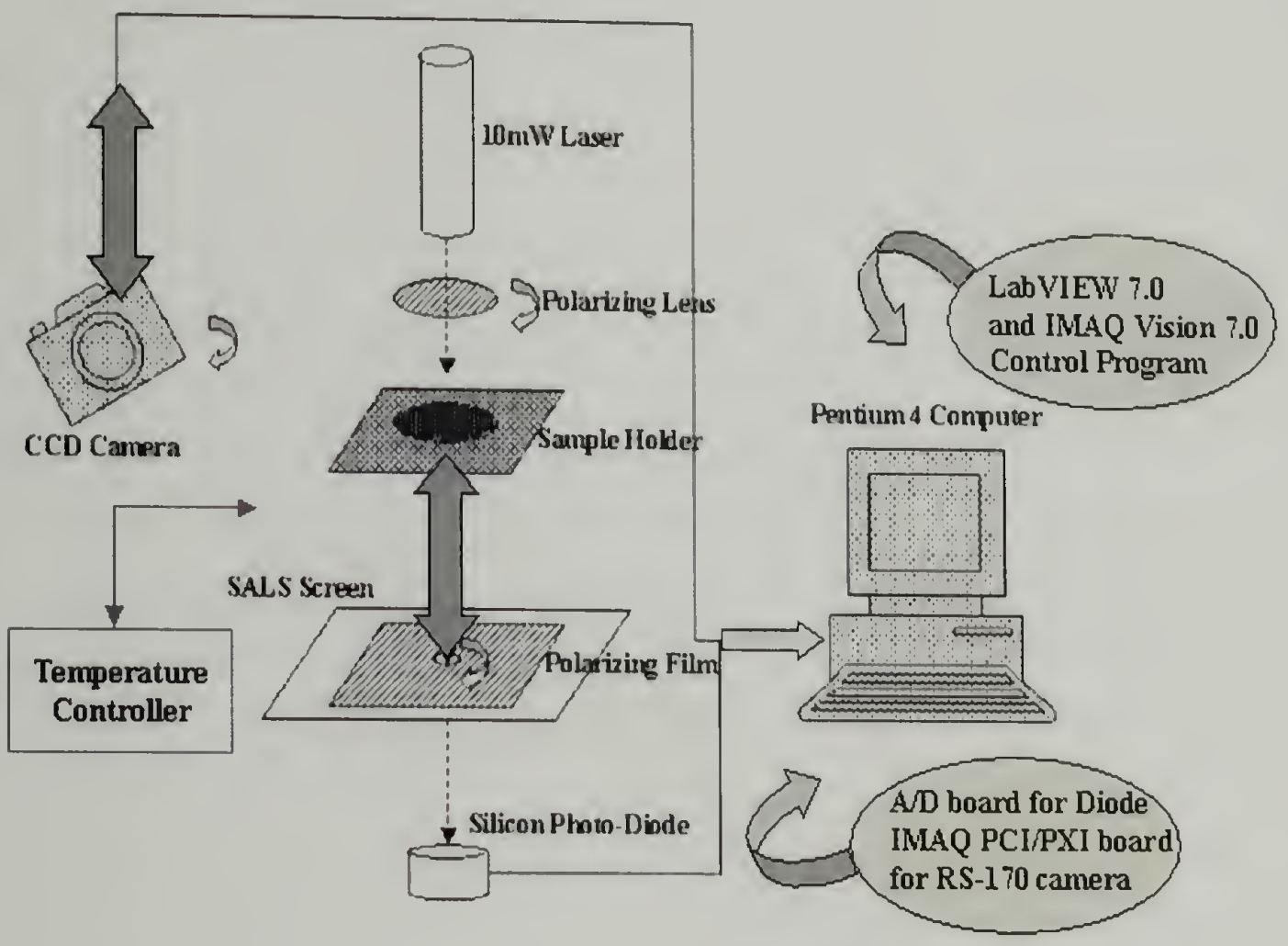

Figure 3.1. Schematic of our Small Angle Light Scattering (SALS) system we built for the polyethylene studies. The camera, sample holder, and screen can be moved along a vertical track. A temperature controller is interfaced with the sample holder. A calibration is performed to compensate for the offset position of the camera.

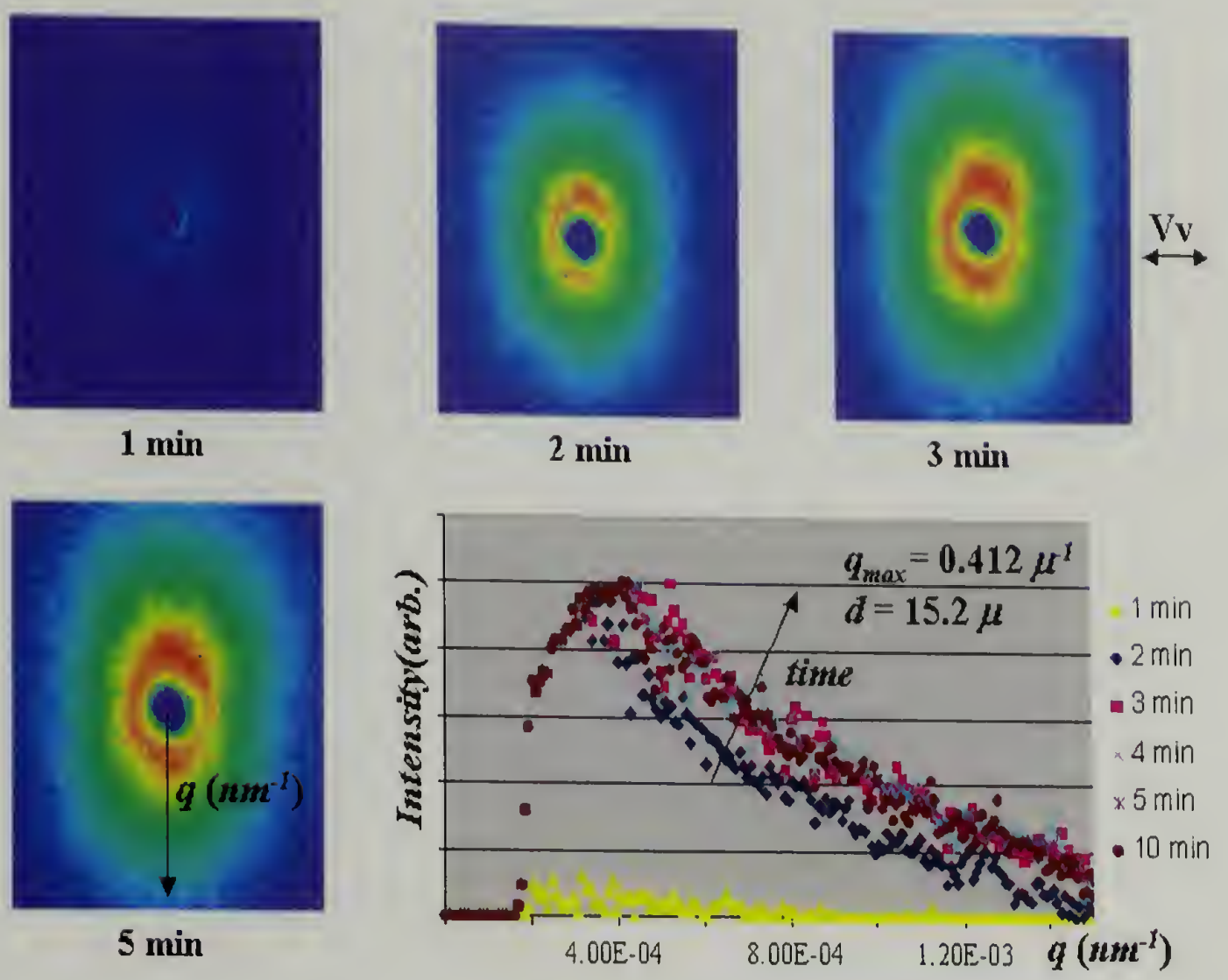

Figure 3.2. Vertical-vertical (Vv) SALS patterns are shown as a function of time. Intensity versus q is also shown as a function of time. Scattering patterns for 0.05 wt.% PE in *para*-xylene quenched at 65°C. Intensity versus q along the direction depicted with the arrow. The maximum of q is shown for the 10 min. plot and $d = 2\pi/q_{max}$.

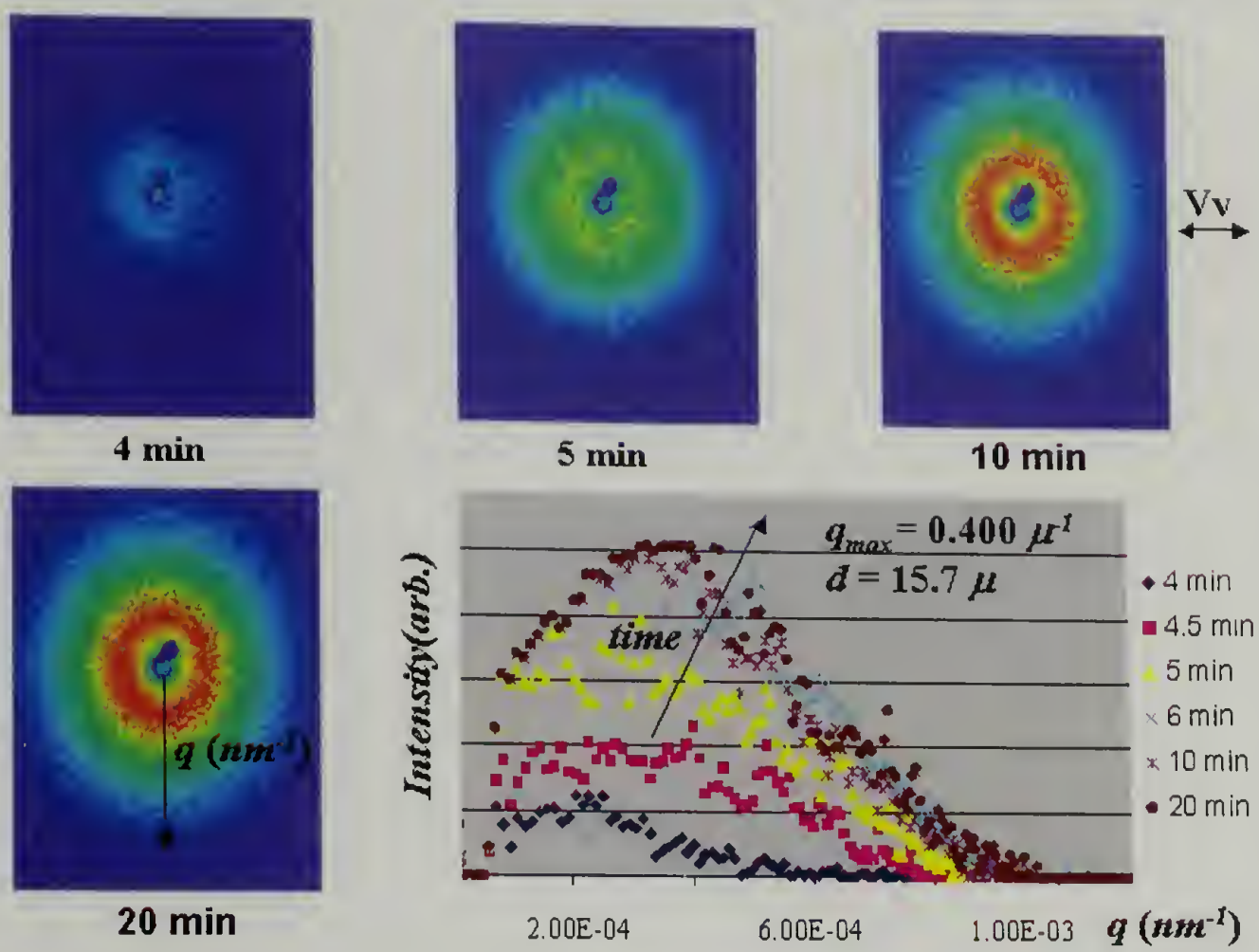

Figure 3.3. Vertical-vertical (Vv) SALS patterns are shown as a function of time. Intensity versus q is also shown as a function of time. Scattering patterns for 0.05 wt.% PE in *para*-xylene quenched at 80°C. Intensity versus q along the direction depicted with the arrow. The maximum of q is shown for the 20 min. plot and $d = 2\pi/q_{max}$.

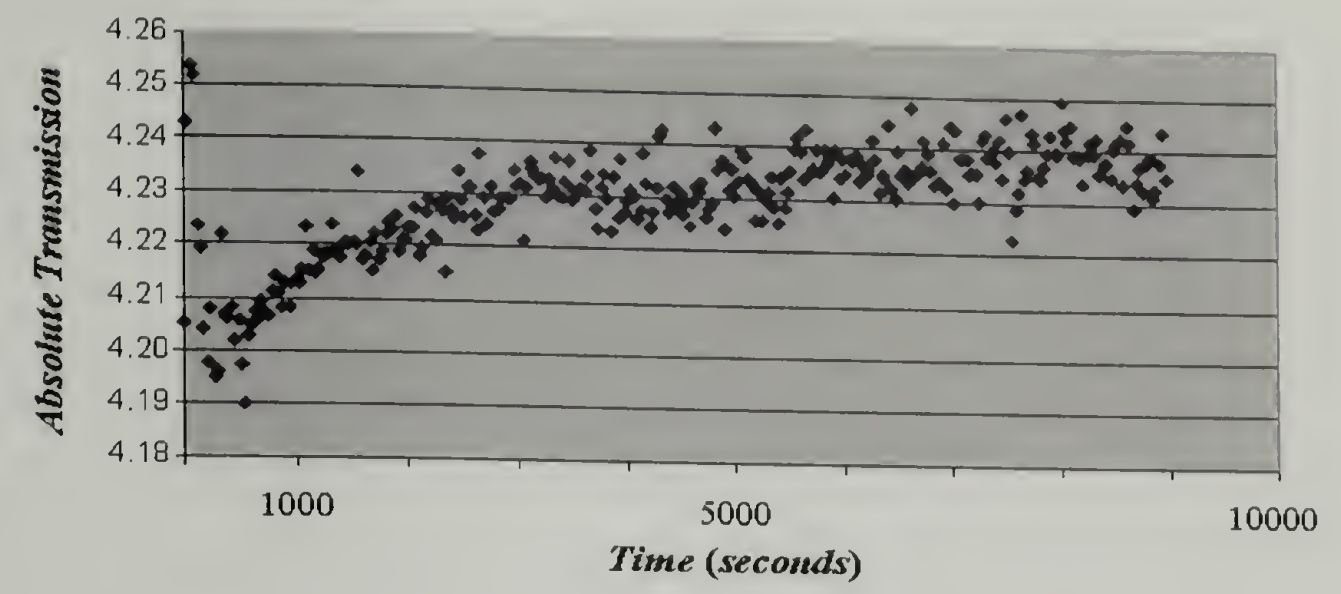

Figure 3.4 Absolute transmission of the sample as a function of time. Transmission of main beam for 0.05 wt.% PE in *para*-xylene quenched at 65°C.

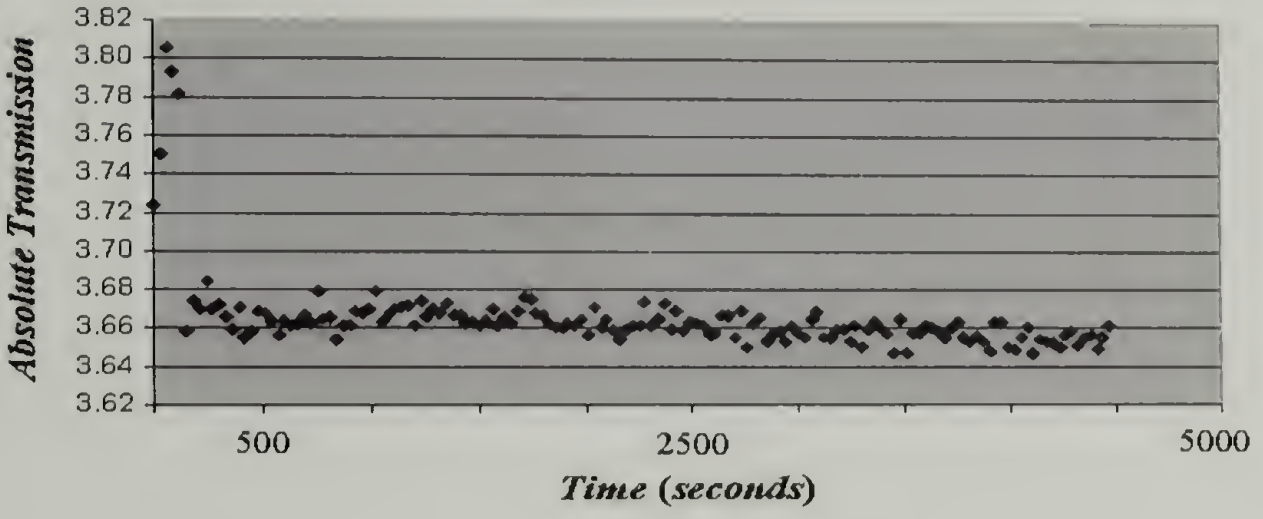

Figure 3.5. Absolute transmission of the sample as a function of time. Transmission of main beam for 0.05 wt.% PE in *para*-xylene quenched at 80°C.

Figure 3.6. TEM of the quenched crystals after evaporation of the solvent. TEM for 0.05 wt.% PE in *para*-xylene quenched at 65°C.

Figure 3.7. TEM of the quenched crystals after evaporation of the solvent. TEM for 0.05 wt.% PE in *para*-xylene quenched at 80°C.

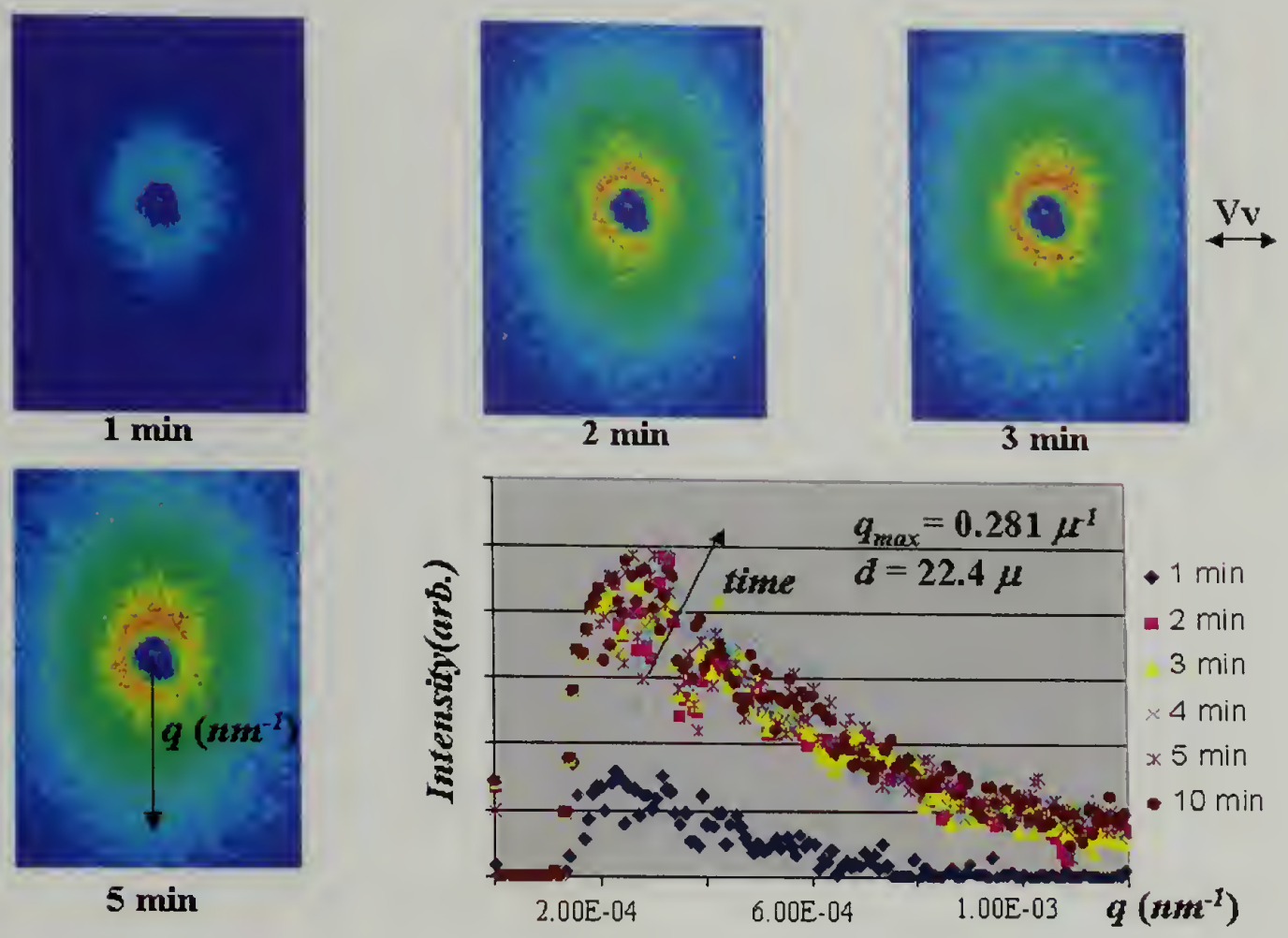

Figure 3.8. Vertical-vertical (Vv) SALS patterns are shown as a function of time. Intensity versus q is also shown as a function of time. Scattering patterns for 0.05 wt.% PE in *para*-xylene quenched at 60°C. Intensity versus q along the direction depicted with the arrow. The maximum of q is shown for the 10 min. plot and $d = 2\pi/q_{max}$.

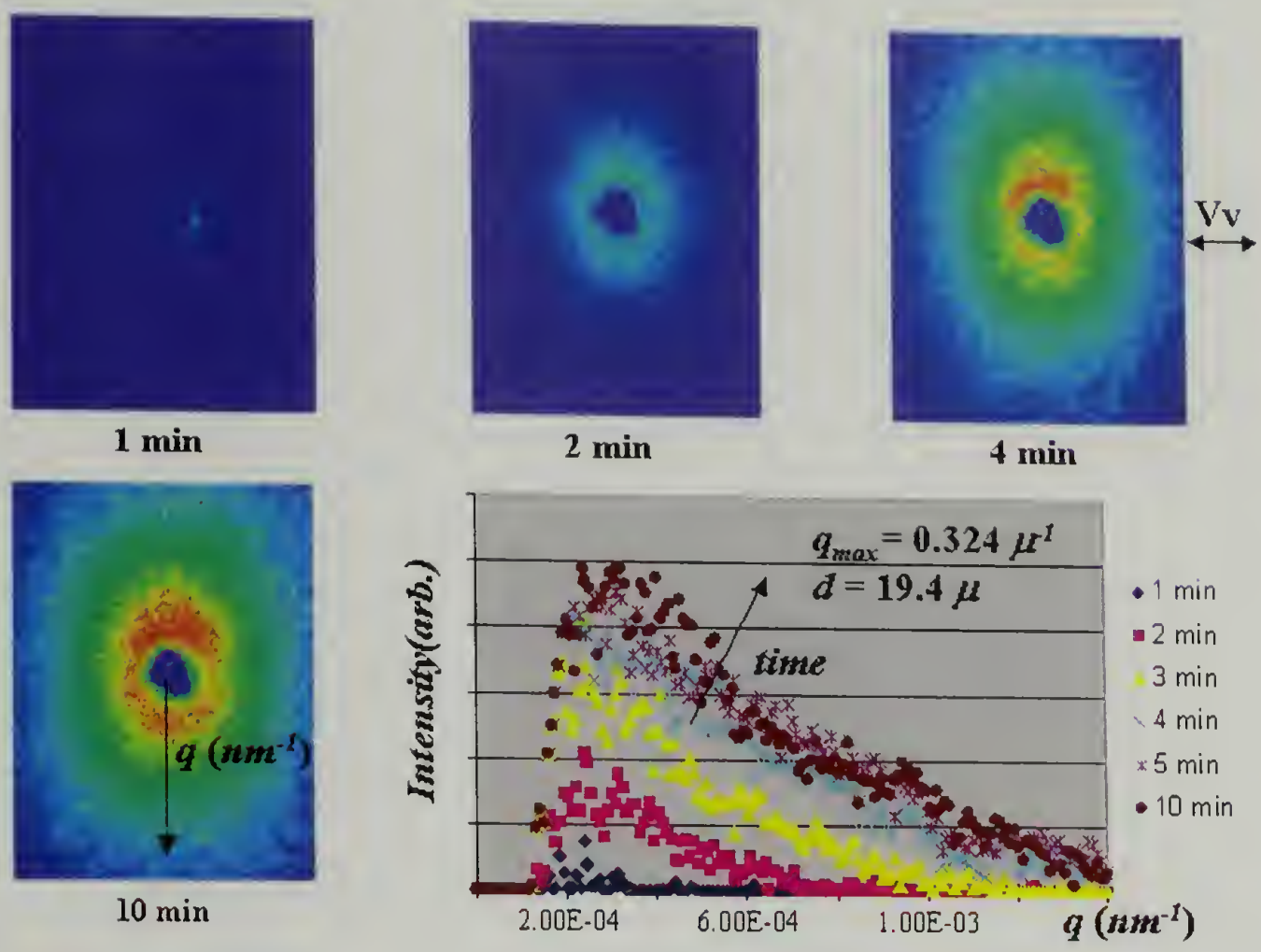

Figure 3.9. Vertical-vertical (Vv) SALS patterns are shown as a function of time. Intensity versus q is also shown as a function of time. Scattering patterns for 0.05 wt.% PE in *para*-xylene quenched at 70°C. Intensity versus q along the direction depicted with the arrow. The maximum of q is shown for the 10 min. plot and $d = 2\pi/q_{max}$.

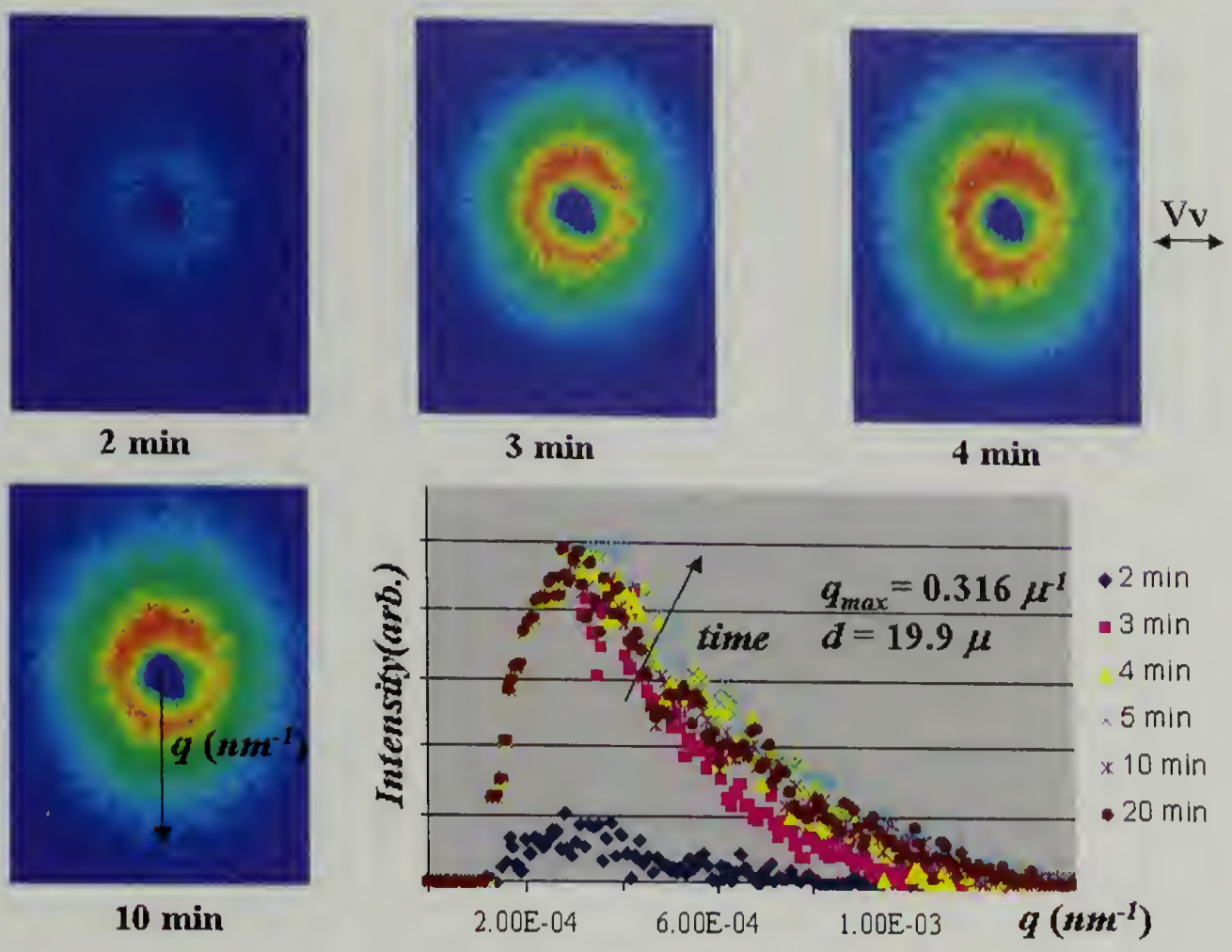

Figure 3.10. Vertical-vertical (Vv) SALS patterns are shown as a function of time. Intensity versus q is also shown as a function of time. Scattering patterns for 0.05 wt.% PE in *para*-xylene quenched at 75°C. Intensity versus q along the direction depicted with the arrow. The maximum of q is shown for the 20 min. plot and $d = 2\pi/q_{max}$.

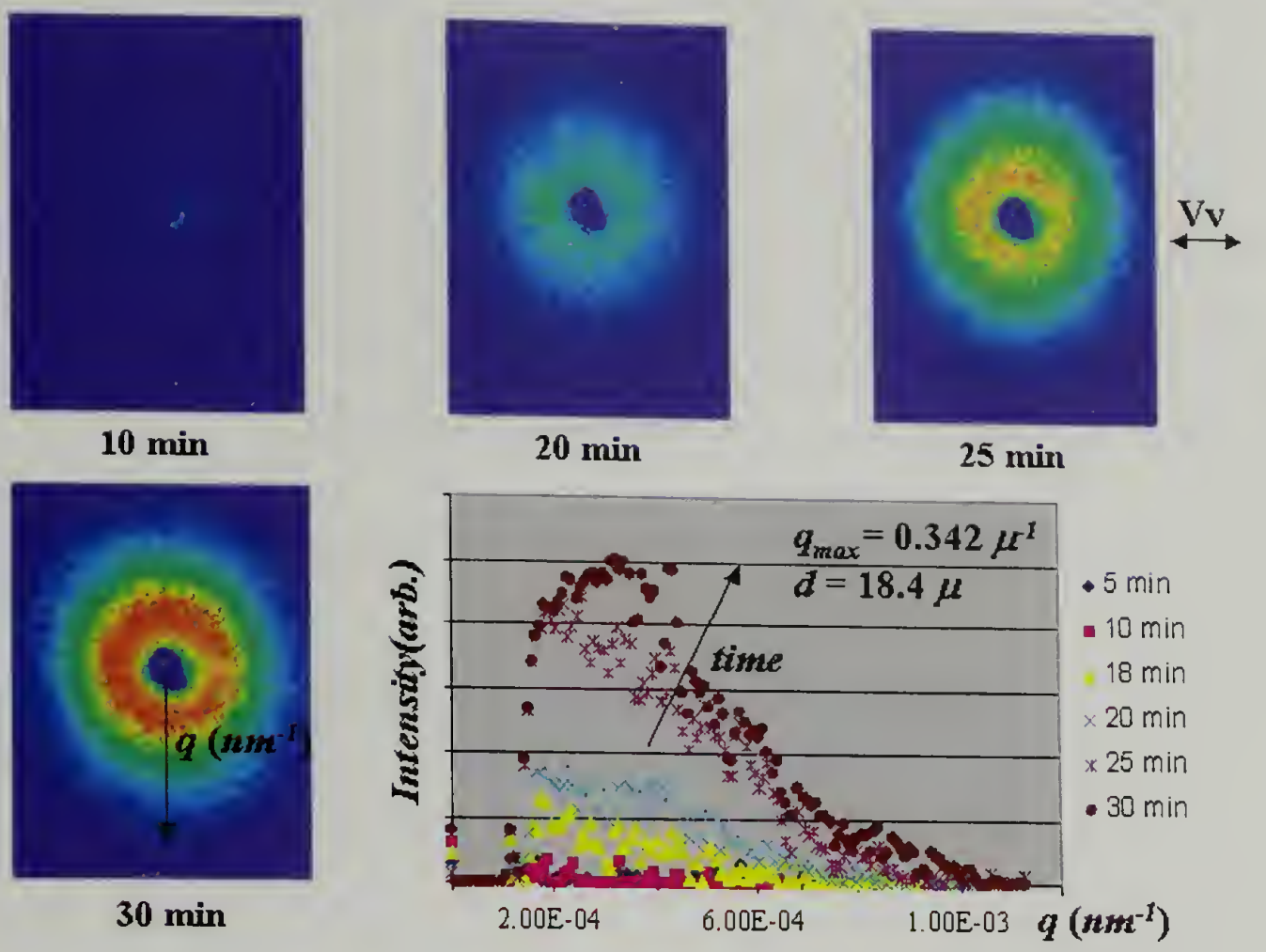

Figure 3.11. Vertical-vertical (Vv) SALS patterns are shown as a function of time. Intensity versus q is also shown as a function of time. Scattering patterns for 0.05 wt.% PE in *para*-xylene quenched at 85°C. Intensity versus q along the direction depicted with the arrow. The maximum of q is shown for the 30 min. plot and $d = 2\pi/q_{max}$.

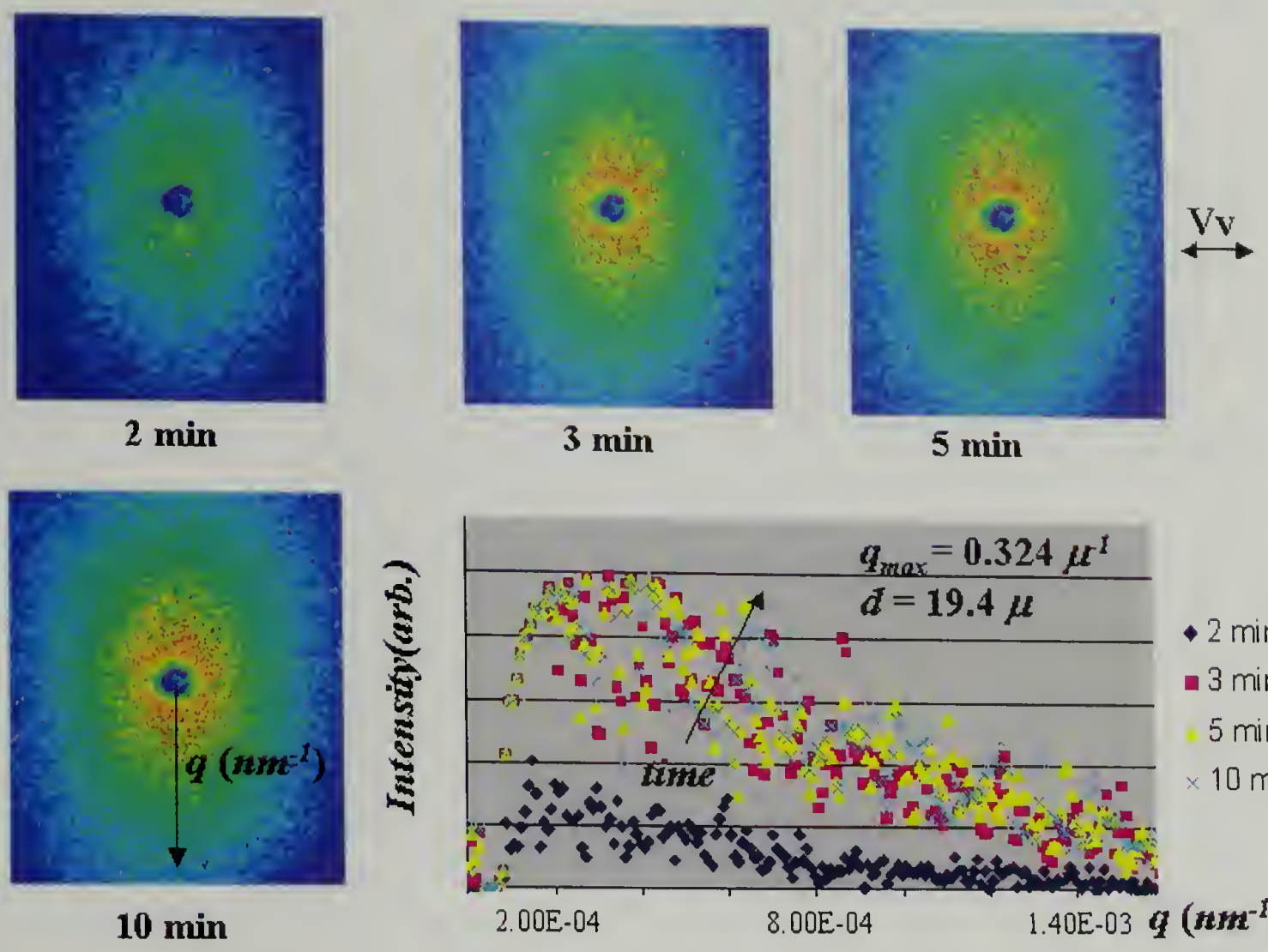

Figure 3.12. Vertical-vertical (Vv) SALS patterns are shown as a function of time. Intensity versus $\boldsymbol{q}$ is also shown as a function of time. Scattering patterns for 0.1 wt.% PE in *para*-xylene quenched at 65°C. Intensity versus $\boldsymbol{q}$ along the direction depicted with the arrow. The maximum of $\boldsymbol{q}$ is shown for the 10 min. plot and $d = 2\pi/q_{max}$.

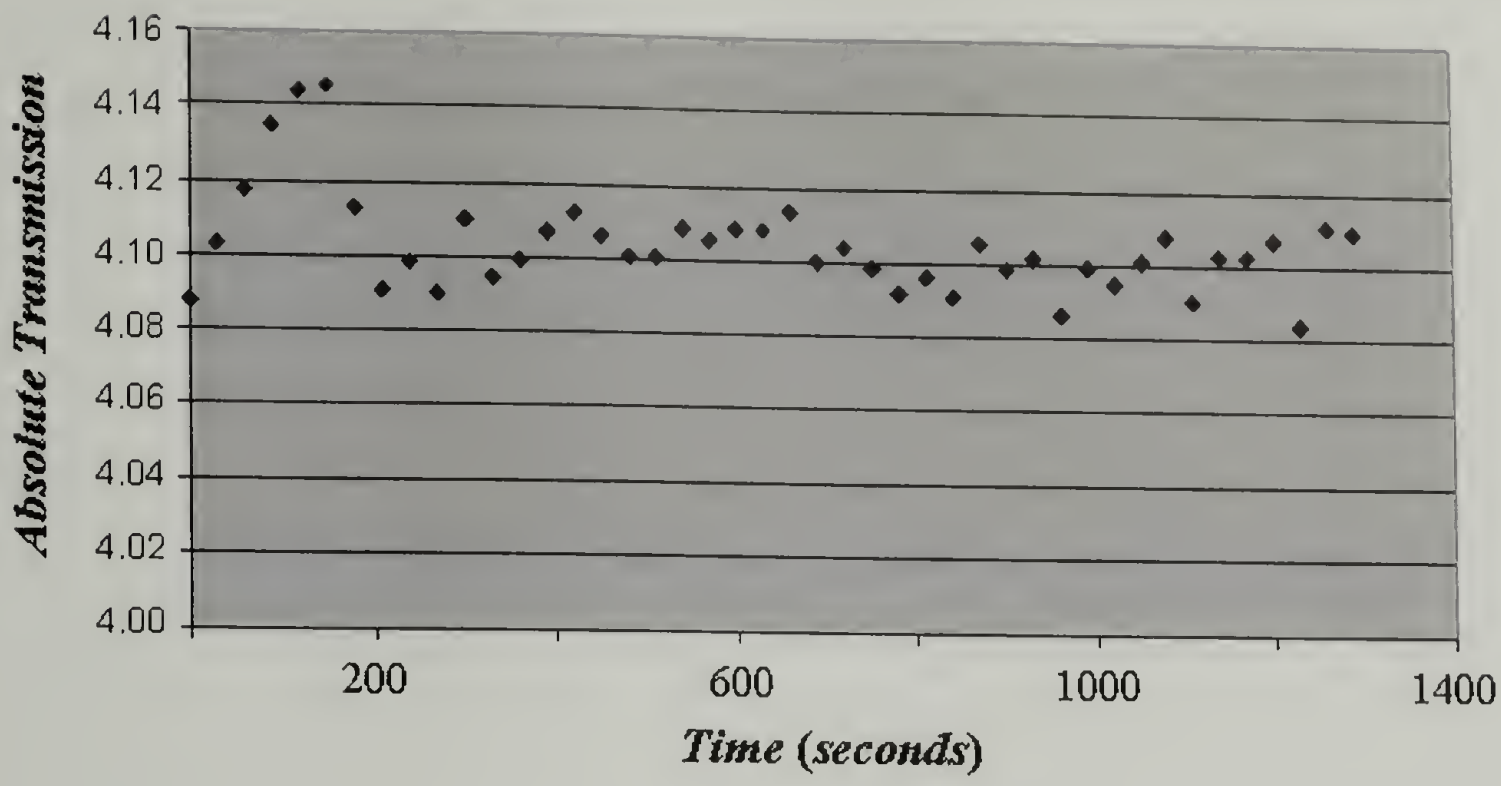

Figure 3.13. Absolute transmission of the sample as a function of time. Transmission of main beam for 0.1 wt.% PE in *para*-xylene quenched at 65°C.

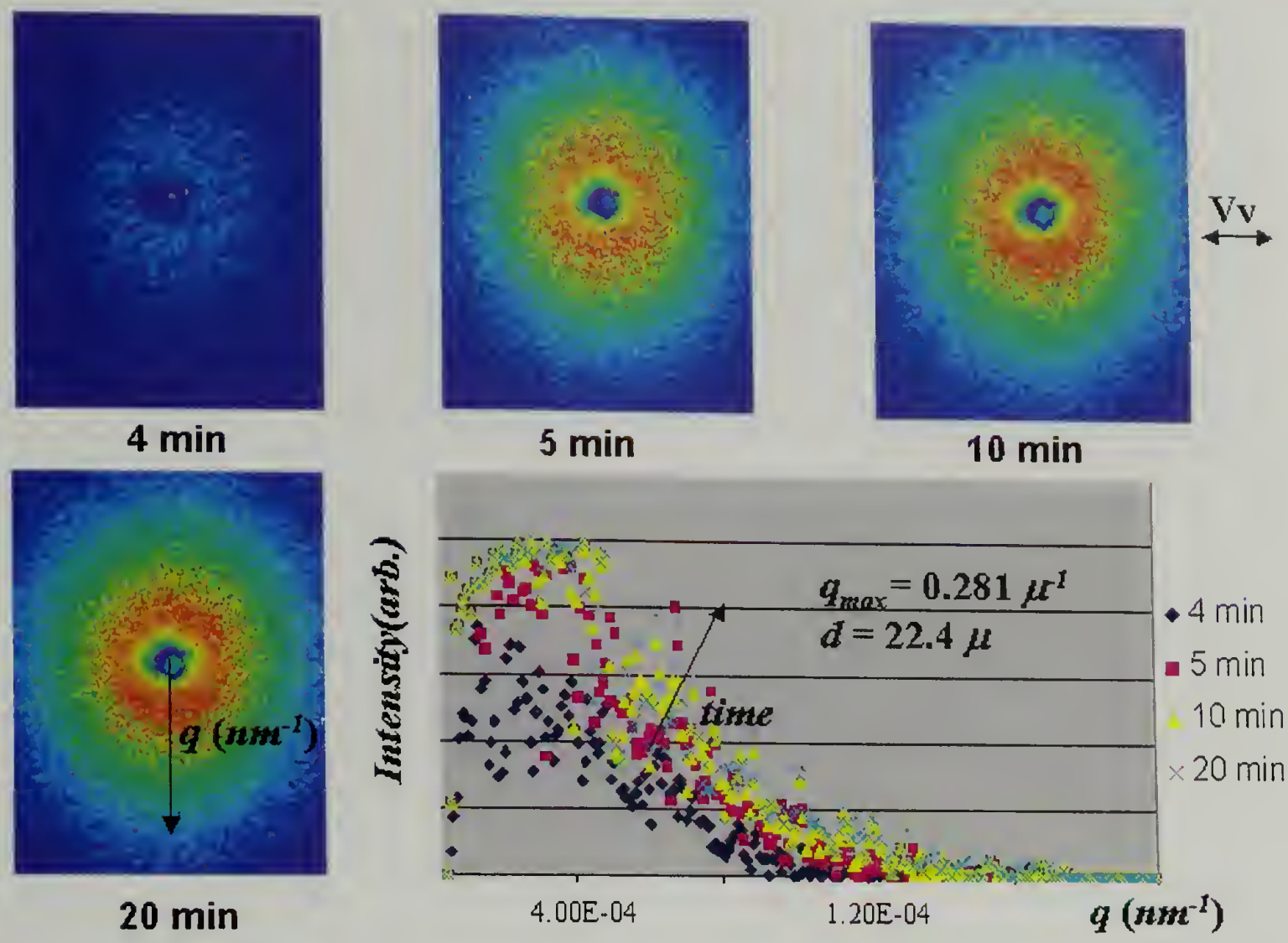

Figure 3.14. Vertical-vertical (Vv) SALS patterns are shown as a function of time. Intensity versus q is also shown as a function of time. Scattering patterns for 0.1 wt.% PE in *para*-xylene quenched at 80°C. Intensity versus q along the direction depicted with the arrow. The maximum of q is shown for the 20 min. plot and $d = 2\pi/q_{max}$.

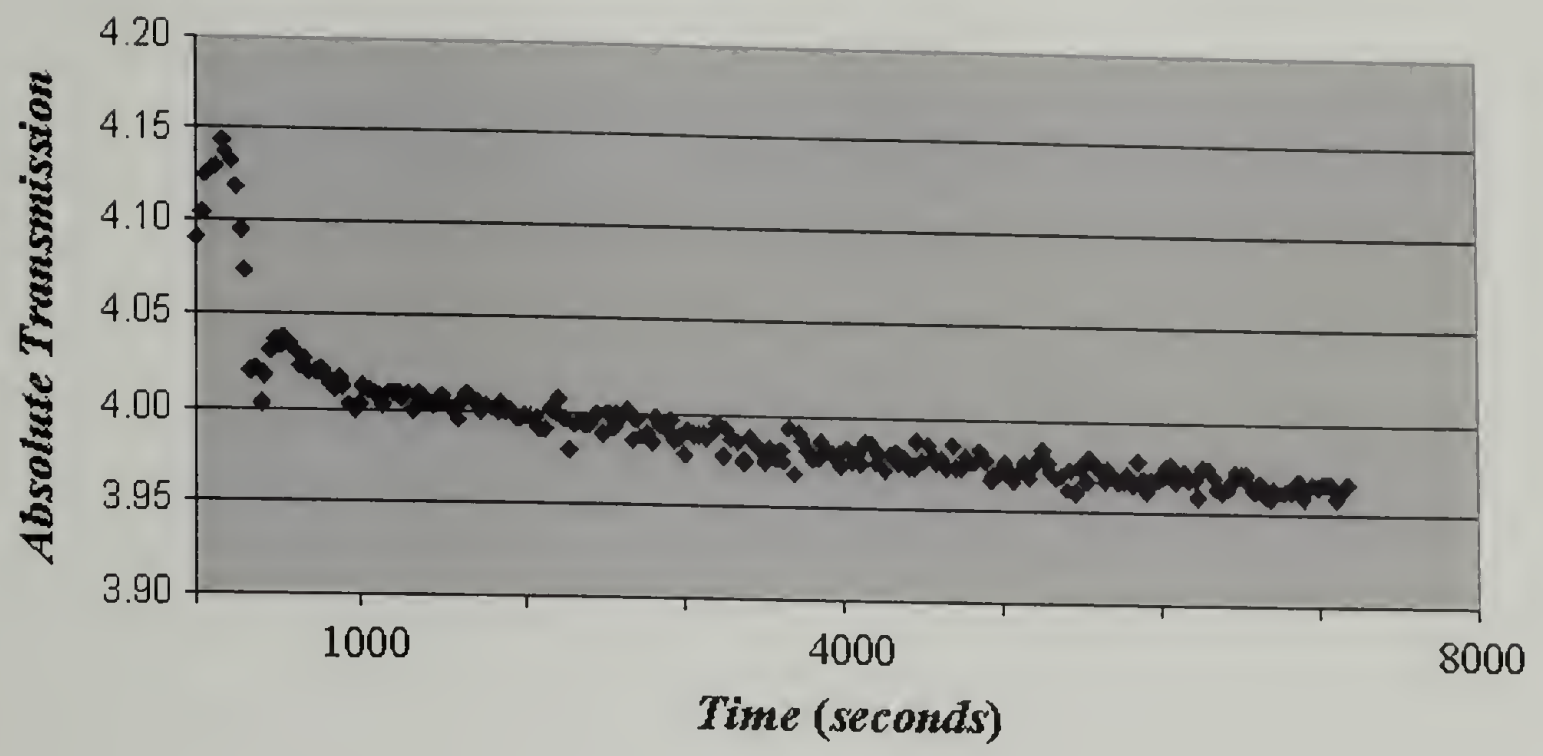

Figure 3.15. Absolute transmission of the sample as a function of time. Transmission of main beam for 0.1 wt.% PE in *para*-xylene quenched at 80°C.

CHAPTER 4

DYNAMIC LIGHT SCATTERING STUDIES OF PEO AND NAPSS AGGREGATION WITH DIVALENT SALT

4.1 Introduction

The aggregation of polyelectrolytes in aqueous solutions is a fundamental phenomenon in polymer science. From previous studies, we know that a second diffusional mode appears in polyelectrolyte systems as the polymer concentration increases or as the ionic strength decreases [44,46]. This slow mode corresponds to the diffusion of large polymer aggregates. It is thought that the presence of impurities like salt [41], hydrogen bonding [42], or triple screening associated with hydrodynamic effects [43] is responsible for these aggregates. Aggregation with uncharged water-soluble polymers like poly(ethylene-oxide) (PEO) or poly-ethylene-glycol (PEG), leading to heterogeneous diffusion coefficients, has also been reported, although the aggregation mechanism is unknown [51-53].

The ratio of polymer concentration (g/L) to salt concentration (mol/L) λ (g/mol) is used to characterize the diffusional dynamics of polymer/salt systems. Generally, only one mode is seen for $\lambda < 1$ g/mol, while a second slow mode appears when $\lambda > 1$ g/mol. The transition at $\lambda \cong 1$ g/mol is generally referred to as the ordinary-extraordinary transition. Although uncharged polymers like PEO or PEG do experience an ordinary-extraordinary transition, there is no single parameter that delineates the two regions.

The first detailed studies of polyelectrolyte/salt systems and the ordinary-extraordinary transition were done with poly(2-vinylpyridine) and potassium bromide [44]. These studies used static (SLS) and dynamic light scattering (DLS) and covered a large range of polymer and salt concentrations. Sodium-poly(styrene-sulfonate) (NaPSS) aggregation has been studied without salt [45], with NaCl [46], and multivalent salts [47]. The effects of molar mass and polymer concentration on aggregates have also been investigated [48]. PEO aggregation has been studied mostly without added salt [49-53] and these aggregates have been shown to be very stable, although the phase transition properties in this system have been studied with NaCl [54]. However, it has been reported that PEO can be prepared in water without added salt so that aggregates will not form [50].

We study NaPSS and PEO aggregation with added divalent salt and the polymer concentration dependence of the fast mode diffusion coefficient (D_{fast}) and the slow mode diffusion coefficient (D_{slow}). Using DLS, we measure D_{fast} and D_{slow} of NaPSS and PEO in the dilute regime with added $BaCl_2$. As far as we know, this is the first time PEO aggregation has been studied with added divalent $BaCl_2$. We cover the concentration regime of 0.025-0.75 g/L for NaPSS with 0.01M and 0.025-2.5 g/L for PEO with 0.025M of $BaCl_2$. We find that the diffusion coefficients remain relatively constant in the concentration regimes investigated and the fast mode and slow mode for both polymers differ by about 1½ orders of magnitude: 1.1×10^{-6} cm^2/s versus 7.8×10^{-8} cm^2/s for NaPSS and 6.7×10^{-7} cm^2/s versus 4.2×10^{-8} cm^2/s for PEO.

We also study PEO without salt in a more concentrated regime and calculate the hydrodynamic radii of aggregates and single chains with a polymer-concentration-

dependent viscosity. These calculations result in a very stable aggregate radius: 45 nm for 49,000 g/mol PEO and 55 nm for the 96,000 g/mol PEO. We also saw a sharper decrease in single chain radii, 5 nm down to 1 nm, with increasing PEO concentration compared to calculations using the viscosity of water at 25°C.

Studying how aggregation of NaPSS and PEO depends on their concentration can help elucidate the micellization behavior of PEO/NaPSS diblocks. Similar studies have been done on polystyrene/poly(ethylene-oxide) diblocks [55,56] with one hydrophobic block and one hydrophilic block, and also PE/NaPSS diblocks [57] with one hydrophobic block and one charged block. These studies have found the formation of micelles with hydrophobic cores and outer hydrophilic coronas in aqueous solution. Measurements were made of molecular weights, radii of gyration, hydrodynamic radii, core and corona radii and diffusion coefficients for the micelles [55-57].

This chapter is organized as follows: the materials and methods are explained in Sec. 2; our results are given in Sec. 3; the conclusions are summarized in Sec. 4.

4.2 Sample Preparation and Dynamic Light Scattering

We used NaPSS that was sulfonated in-house from narrow molecular weight polystyrene with a polydispersity of 1.02. Vivek Prabhu of the M. Muthukumar research group at the Polymer Science and Engineering Department, University of Massachusetts, Amherst performed the sulfonation. The polystyrene was sulfonated by a method similar to that described by H. Vink [58]. The sample used had a weight-averaged molecular weight of 120,000 g/mol with a polydispersity of 1.19, as found

by GPC, and was 86-89% sulfonated as determined by elemental analysis (EA). The two PEO samples, #P2472-EO and #P1585-EO, were purchased from Polymer Source, Inc. and had weight-averaged molecular weights of 49,000 and 96,000 g/mol and PDI of 1.09 and 1.04, respectively. This was determined from size exclusion chromatography (SEC) performed by Polymer Source, Inc.

The salt used for our studies was $BaCl_2$ with a molecular weight of 208.23 g/mol, purchased from J. T. Baker Chemical Co. The salt was desiccated overnight to remove all residual water for more accurate weighing. While we also tried NaCl for our aggregation studies, we report data only for $BaCl_2$. The monovalent salt did not produce a consistent slow mode for all runs with the polymers we studied.

The solvent for all of our studies was purified RO water de-ionized with a Milli-Q UF Plus purification system having a final resistance of 18MΩ as determined by the purification system. The tubes used for DLS were 10 × 75 mm culture tubes, #14-961-25, from Fisher Scientific. The caps used were TainerTop safety closures from Fisher Scientific.

A cleaning regimen was established to ensure that the solutions and the culture tubes were free of contaminants. Tubes were cleaned in batches of 12 to 15. All tubes were rinsed with a low-residue cleaning solution of 2% Micro90 from Cole-Parmer in purified RO water de-ionized with a Milli-Q purification system. Then the tubes were put in a Branson 2510 sonicator bath with the cleaning solution, and then rinsed several times with de-ionized water. All tubes were filled with acetone and put in an acetone filled beaker, then covered with Parafilm. This was done to control dust.

Stock solutions of the purified/de-ionized water with added salt were made and stored in Pyrex 140°C jars. 0.01 M and 0.025 M $BaCl_2$ solutions were made and used for the polymer solutions. To make the polymer solutions, salt solution was measured into disposable scintillation vials (20mL) and the appropriate amount of polymer was added. We made polymer concentrations of 0.025, 0.05, 0.1, 0.2 and 0.75 g/L for NaPSS and 0.025, 0.05, 0.1, 0.2, 0.625, 1.25 and 2.5 g/L for PEO. All polymer solutions were made immediately prior to DLS and only the stock salt solutions were kept for any length of time.

Polymer solutions were filtered with 3 mL sterile single-use syringes through Millipore GS 0.2μ pore-sized syringe filters into clean borosilicate-glass tubes, which had previously been removed from acetone bath and dried with a purified-air duster. The tubes were filled with between 2-2.5 mL of the polymer/salt solution. After filling the tubes with polymer and salt solution, we capped them with the safety closures. The outside of the filled tube was rinsed with acetone and dusted with purified-air before placing them into the DLS sample holder.

DLS is a tool to measure fluctuations in scattered light intensity and determine the diffusion coefficients of species in solution. When this is done in the dilute regime, as in our case, the cooperative diffusion coefficients measured are the same as the tracer or self-diffusion coefficients. Photons are detected with a photo-multiplier tube and their signal then goes through a pulse amplifier and then an auto-correlator. Measurements depend on the magnitudes of the scattering wave vectors k,

$$k = \frac{4\pi}{\lambda} \sin\theta/2 \ . \qquad (4.2.1)$$

For a diffusive process, the time-dependent density autocorrelation function for k is related to the diffusion coefficient through:

$$\langle \rho_k(t)\rho_{-k}(0)\rangle = (const.)e^{-Dk^2t}. \qquad (4.2.2)$$

This function is identical to the normalized time-dependent electric field autocorrelation function $g_1(\tau)$ arising in the theoretical treatment of particle scattering:

$$g_1(\tau) = \langle E(\tau)E(0)\rangle / \langle E(0)E(0)\rangle . \qquad (4.2.3)$$

The Siegert relation provides a connection between $g_1(\tau)$ and the normalized time-dependent intensity autocorrelation function $g_2(\tau)$ which is measured with DLS:

$$g_1(\tau)^2 = g_2(\tau) - 1. \qquad (4.2.4)$$

The CONTIN software fits this intensity autocorrelation function as a sum of exponentials to produce a weighted distribution of the exponential decay times. The fast mode decay time τ_{fast} and the slow mode decay time τ_{slow} are used to calculate the diffusion coefficients through:

$$1/\tau_{fast,slow} = D_{fast,slow}\, k^2 . \qquad (4.2.5)$$

Plotting $1/\tau$ versus k^2 for multiple angles by rotating the detector with a precision goniometer yields the diffusion coefficient as the slope of equation 4.2.5.

We used the ALV 5000 static and dynamic light scattering apparatus in the D. Hoagland research group at the Polymer Science and Engineering Department, University of Massachusetts, Amherst. This unit was equipped with an Innova-70 argon laser (514.5 nm and 3W max. power) from Coherent Inc., an ALV/SP-125 precision goniometer, a photo-multiplier tube from Thorn EMI Electron Tubes, and

signal processing was done with an ALV 5000 Multiple Tau Digital Correlator board and CONTIN software.

Measurements were made for 0.025, 0.05, 0.1, 0.2 and 0.75 g/L solutions of NaPSS in 0.01 M $BaCl_2$. A fast mode and slow mode were detected for all these concentrations. Measurements were also made for 0.025, 0.05, 0.1, 0.2, 0.625, 1.25 and 2.5 g/L solutions of PEO in 0.025 M $BaCl_2$. A fast mode and slow mode were detected for all these concentrations. All DLS measurements were done for angles of 30°, 45° and 60° defining three scattering wave vectors. Data were discarded if the linear fit to equation 4.2.5 of the three data points, corresponding to the three angles, did not pass close to the origin of the plot. A toluene calibration curve is not needed for dynamic light scattering unlike static light scattering.

The magnitudes of scattering wave vectors were calculated from equation 4.2.1 using the known angles and the laser wavelength.. The diffusion coefficients were calculated for NaPSS and PEO at temperatures of 30°C and 25°C, respectively. From the values of D_{fast} and D_{slow} we calculated the hydrodynamic radii using the Stokes-Einstein relation as in Fig. 4.1.

4.3 Slow Mode and Fast Mode Results

4.3.1 120,000 g/mol NaPSS

The analysis of 0.025 g/L NaPSS data resulted in a D_{fast} of 9.32×10^{-7} cm^2/s and a D_{slow} of 6.45×10^{-8} cm^2/s. 0.05 g/L NaPSS yielded a fast mode of 1.57×10^{-6} cm^2/s and a slow mode of 5.08×10^{-8} cm^2/s. A 0.1 g/L solution of NaPSS yielded a

fast mode of 1.10×10^{-6} cm^2/s and a slow mode of 7.75×10^{-8} cm^2/s. The analysis of 0.2 g/L NaPSS yielded a D_{fast} of 9.12×10^{-7} cm^2/s and a D_{slow} of 6.09×10^{-8} cm^2/s. Finally, the 0.75 g/L NaPSS gave us a fast mode of 9.01×10^{-7} cm^2/s and a slow mode of 4.65×10^{-8} cm^2/s. Overall, in our concentration regime, D_{fast} remained constant at about 1.1×10^{-6} cm^2/s and D_{slow} remained constant at about 7.8×10^{-8} cm^2/s.

These data were superimposed on data from Forster et al. [44] for 109,000 g/mol weight-averaged poly (2-vinylpyridine) in 0.01 M KBr as shown in Fig. 4.2. Our data lined up well for both the fast mode and slow mode, although we were not able to make measurements near the ordinary-extraordinary transition. Our values of λ were 2.5, 5, 10, 20 and 75 g/mol. For $\lambda < 1$ g/mol, only the fast mode is seen for polyelectrolyte and salt systems. 0.025 g/L was the lowest NaPSS concentration we were able to study with DLS.

4.3.2 49,000 g/mol PEO

Our analysis of 0.025 g/L PEO resulted in a D_{fast} of 4.16×10^{-7} cm^2/s and a D_{slow} of 3.29×10^{-8} cm^2/s. 0.05 g/L PEO gave a fast mode of 5.96×10^{-7} cm^2/s and a slow mode of 2.59×10^{-8} cm^2/s. A 0.1 g/L solution of PEO yielded a fast mode of 4.58×10^{-7} cm^2/s and a slow mode of 5.35×10^{-8} cm^2/s. The analysis of 0.2 g/L PEO yielded a fast mode of 8.52×10^{-7} cm^2/s and a slow mode of 2.59×10^{-8} cm^2/s. 0.625 g/L PEO resulted in a D_{fast} of 6.70×10^{-7} cm^2/s and a D_{slow} of 4.18×10^{-8} cm^2/s. A 1.25 g/L solution of PEO yielded a fast mode of 6.70×10^{-7} cm^2/s and a slow mode of 8.61×10^{-8} cm^2/s. Finally, the 2.5 g/L PEO gave us a fast mode of 7.29×10^{-7} cm^2/s

and a slow mode of 5.32×10^{-8} cm^2/s. Overall, in our concentration regime, D_{fast} remained constant at about 6.7×10^{-7} cm^2/s and D_{slow} remained constant at about 4.2×10^{-8} cm^2/s.

Data were superimposed on the data from Forster et al. [44] for 109,000 g/mol weight-averaged poly (2-vinylpyridine) in 0.01 M KBr as shown in Fig. 4.3. The results of our PEO data lined-up well for both the fast mode and slow mode considering that PEO is not a charged polymer and the $\lambda \cong 1$ g/mol rule for the location of the ordinary-extraordinary transition does not hold. We believe this is the first time PEO aggregation was studied with a divalent salt. Our values of polymer concentration were higher than for NaPSS with 1.25 and 2.5 g/L. The 0.025 g/L PEO was the lowest concentration we were able to study with DLS.

4.3.3 PEO Viscosity Calculations

The diffusion coefficients were used to calculate the hydrodynamic radii from:

$$D_{fast,slow} = \frac{k_B T}{6 \pi \eta_0 R_h}. \qquad (4.3.1)$$

The viscosity of water at 25°C (8.937×10^{-4} Ns/m) was used for these calculations. When we calculated the hydrodynamic radii of the aggregates for 49,000 g/mol PEO without added salt, we found the size doubled, 50nm to 100nm, from lowest to highest polymer concentration.

We expected PEO to have a preferred aggregate size in water without additional salt. We used the Stokes-Einstein relation with a concentration-dependant viscosity to calculate R_h. To do this, we needed the intrinsic viscosity $[\eta]$ and the

Huggins constant h for PEO in water at 25°C. These data are well documented for PEO in the Polymer Handbook and we interpolated values for our molecular weights. These values were used in the Huggins equation:

$$\eta_{sp}/c = h[\eta]^2 c + [\eta] \qquad (4.3.2)$$

which gives the specific viscosity at each concentration. The overall concentration was used for these calculations and not the non-aggregated single chain concentration. These data were not available to us. The results of these calculations for 49,000 g/mol PEO yielded a constant aggregate R_h of about 45 nm as in Fig. 4.4. This was repeated for 96,000 g/mol PEO resulting in a constant aggregate R_h of about 55 nm as in Fig. 4.5. The aggregate R_h for 49,000 g/mol PEO doubled from 50 nm to 100 nm using the water viscosity. The aggregate R_h for 96,000 g/mol PEO almost tripled from 60 nm to 160 nm using the water viscosity.

We also calculated the fast mode R_h using concentration-dependent viscosities. For both 49,000 g/mol and 96,000 g/mol PEO, the hydrodynamic radii of the single chains decreased more rapidly with concentration, compared to calculations using the viscosity of water as shown in Fig. 4.6. The 49,000 g/mol PEO R_h decreased from 3.3nm down to 1.3nm. The 96,000 g/mol PEO R_h decreased from 5.0 nm down to 1.0 nm. Using the viscosity of water at 25°C, the decrease was 21% for the 49,000 g/mol PEO and 36% for the 96,000 g/mol PEO. It is clear from Fig. 4.6, fast mode R_h calculations should be done using the solvent viscosity, not the concentration-dependent solution viscosities.

4.4 Summary and Conclusions

We have reported on diffusion studies of aggregated and single chain species of NaPSS and PEO with added divalent salt. We performed DLS to measure diffusion coefficients for both fast mode and slow mode diffusion of both charged NaPSS and uncharged PEO with $BaCl_2$. These studies were all done in the dilute regime. The D_{fast} and D_{slow} remained relatively constant for both polymers in the 0.025-0.75 g/L regime for NaPSS and in the 0.025-2.5 g/L regime for PEO, differing by about 1½ orders of magnitude: 1.1×10^{-6} cm^2/s versus 7.8×10^{-8} cm^2/s for NaPSS and 6.7×10^{-7} cm^2/s versus 4.2×10^{-8} cm^2/s for PEO. In addition, we calculated the viscosity of PEO in water as a function of increasing polymer concentration without added salt. We used these viscosities to calculate hydrodynamic radii for 1.25, 2.5, 5.0, 7.5, 10 and 15 g/L of the 49,000 and 96,000 g/mol PEO. We found that using a concentration-dependent viscosity in the Stokes-Einstein relation resulted in single chain radii from 5 down to 1 nm and aggregate radii between 45 and 60 nm; using the solvent viscosity resulted in aggregate sizes that almost tripled over the PEO concentrations investigated.

Our results indicate that adding a divalent salt like $BaCl_2$ will produce a consistent slow mode in both NaPSS and PEO for the concentrations investigated. We also found that PEO aggregated without added salt during our sample preparation, and that using the solution viscosity in the Stokes-Einstein relation resulted in more accurate hydrodynamic radii. The increase in viscosity with polymer concentration compensates for the decreasing D_{slow} and results in a constant aggregate size as calculated from the Stokes-Einstein relation. We believe that the presence of ions and single chains in the vicinity of a diffusing species affects the viscosity it experiences.

Based on our results, we hope to extend this work with DLS studies on diblocks of NaPSS and PEO in water with added $BaCl_2$. Using this divalent salt, we expect to see micelles of our PEO/NaPSS diblocks. The size of the micelles, the core radius, and the corona thickness should depend largely on the ionic strength of the solutions and the relative and absolute sizes of the blocks.

$$D_{f,s} = \frac{k_B T}{6 \pi \eta_o R_h}$$

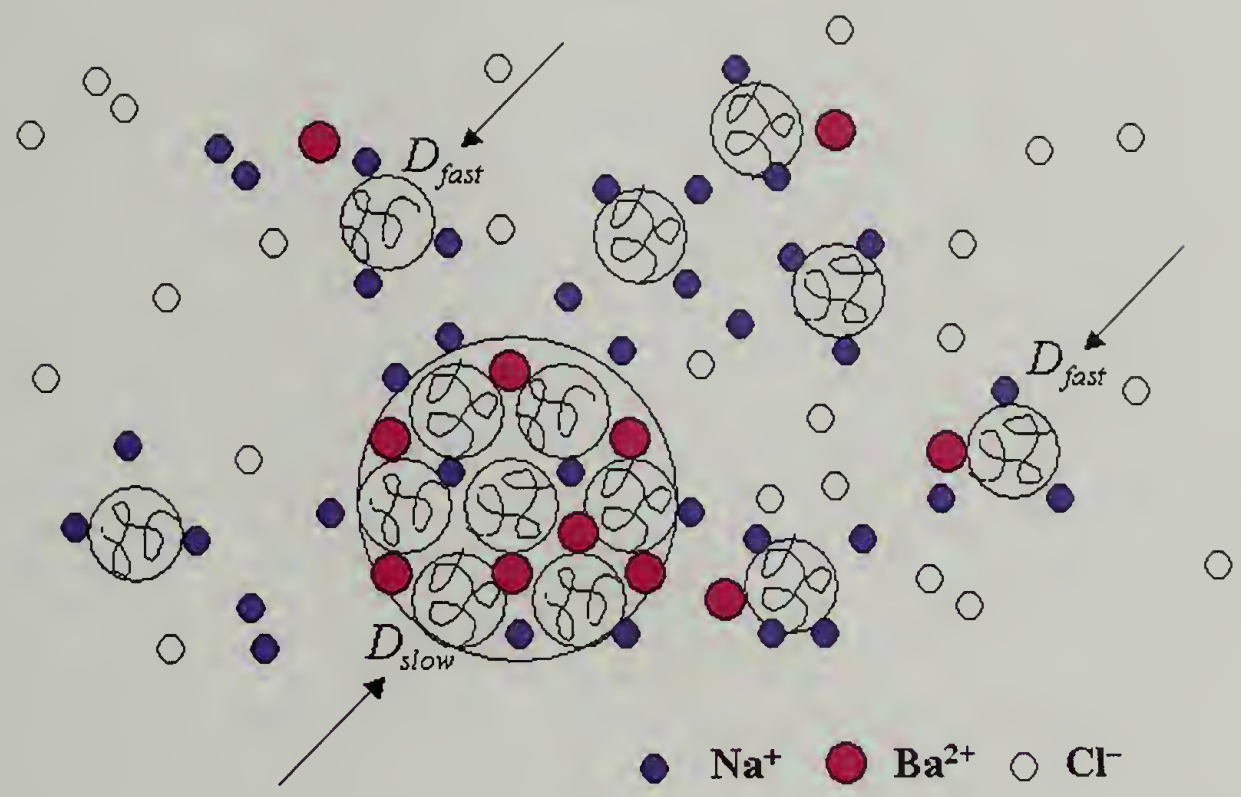

Figure 4.1. The Stokes-Einstein relation for slow mode diffusion coefficient (D_s) and fast mode diffusion coefficient (D_f). A schematic of the slow mode diffusion of aggregates and fast mode diffusion of single chains coupled with sodium, barium and chloride ions.

Conc. (g/L)	D-Slow (cm^2/s)	D-Fast (cm^2/s)	Lambda (C_P/C_S)
0.025	6.45E-08	9.32E-07	2.5
0.05	5.08E-08	1.57E-06	5
0.1	7.75E-08	1.10E-06	10
0.2	6.09E-08	9.12E-07	20
0.75	4.65E-08	9.01E-07	75

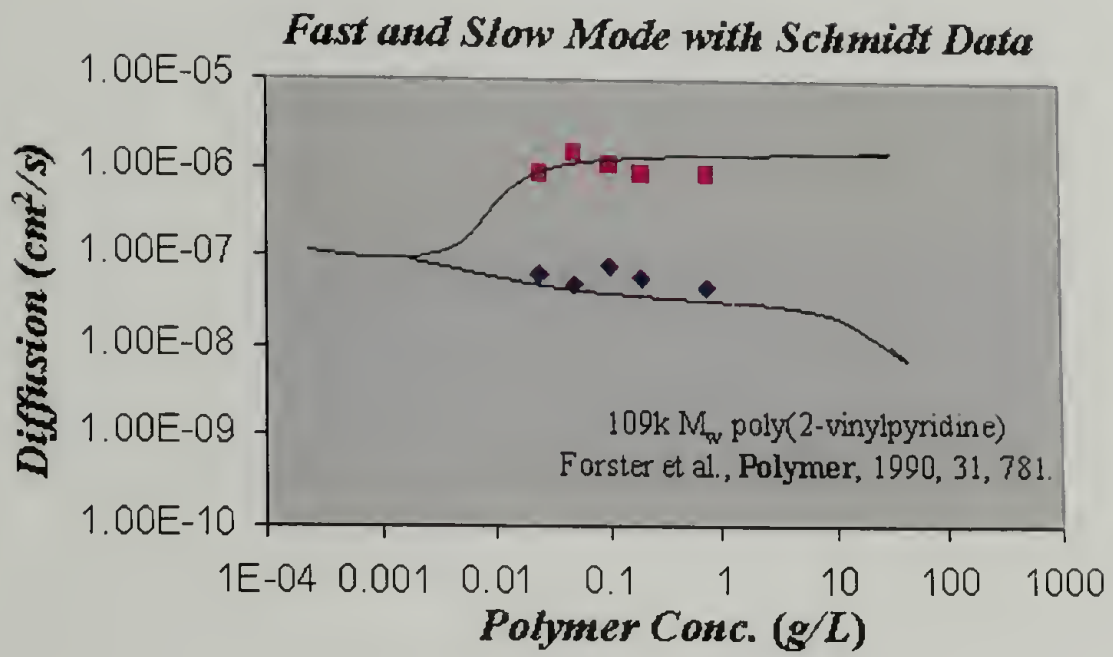

Figure 4.2. Diffusion coefficients versus polymer concentration. D_{slow} and D_{fast} values for NaPSS in 0.01M $BaCl_2$ for various polymer concentrations superimposed on data from Förster et al. [44].

Conc. (g/L)	D-Slow (cm^2/s)	D-Fast (cm^2/s)	Lambda (C_P/C_S)
0.025	3.29E-08	4.16E-07	1
0.05	2.59E-08	5.96E-07	2
0.1	5.35E-08	4.58E-07	4
0.2	2.59E-08	8.52E-07	8
0.625	4.18E-08	6.70E-07	25
1.25	8.61E-08	6.70E-07	50
2.5	5.32E-08	7.29E-07	100

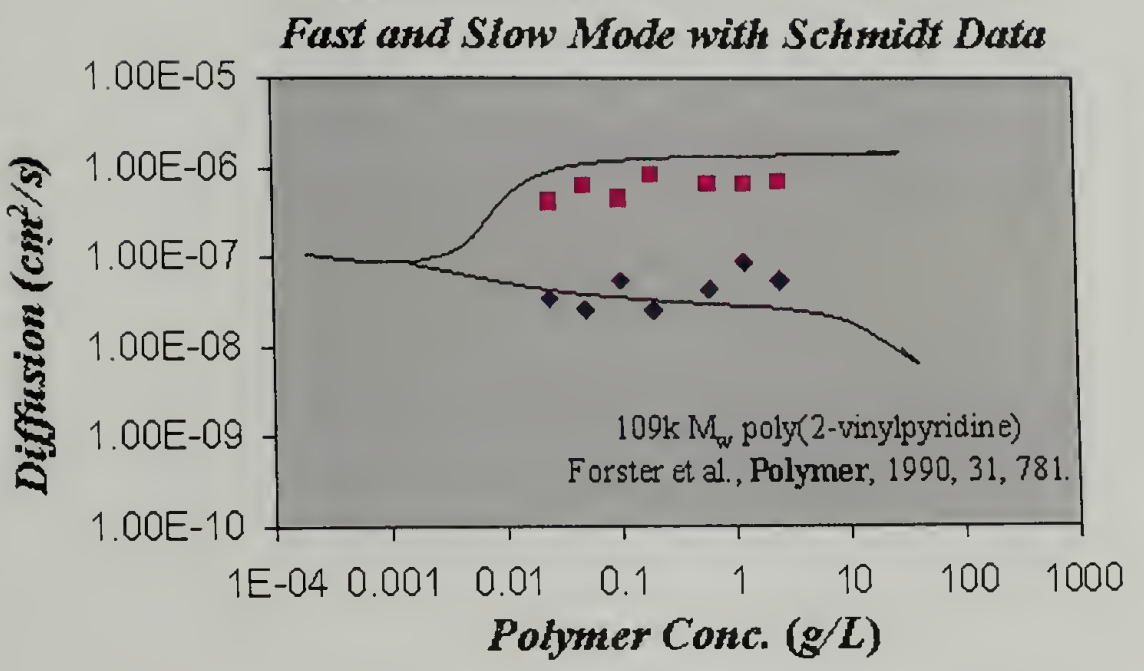

Figure 4.3. Diffusion coefficients versus polymer concentration. D_{slow} and D_{fast} values for PEO in 0.025M $BaCl_2$ for various polymer concentrations superimposed on data from Förster et al. [44].

$$D_s = \frac{k_B T}{6\pi\eta_o R_h}$$

Conc. (g/mL)	D-Slow (m^2/s)	Sol. Visc. (Ns/m^2)
1.25E-03	5.14E-12	9.58E-04
2.50E-03	4.83E-12	1.03E-03
5.00E-03	4.42E-12	1.18E-03
7.50E-03	3.32E-12	1.35E-03
1.00E-02	3.22E-12	1.55E-03
1.50E-02	2.48E-12	1.99E-03

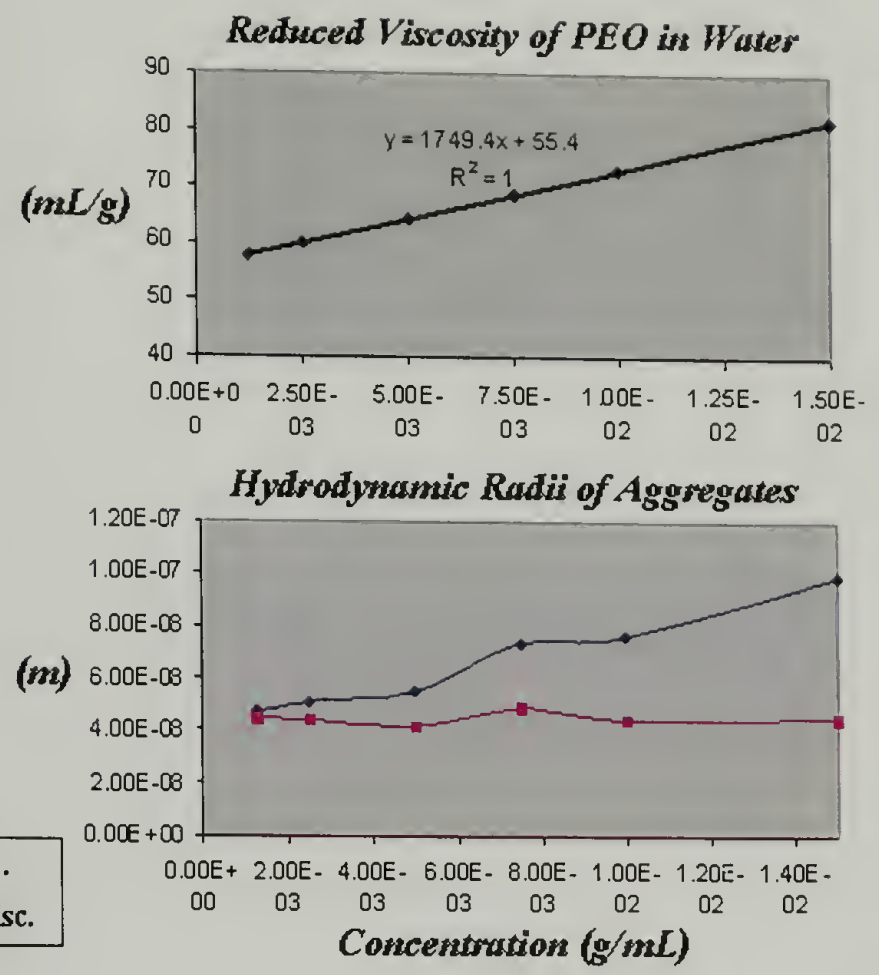

Figure 4.4 Reduced viscosity of PEO in water and aggregate hydrodynamic radii as a function of PEO concentration. Hydrodynamic radii of 49,000 g/mol PEO aggregates with no added salt calculated with (a) the viscosity of water at 25°C and (b) concentration-dependent viscosity of PEO in water at 25°C.

$$D_s = \frac{k_B T}{6\pi\eta_o R_h}$$

Conc. (g/mL)	D-Slow (m^2/s)	Sol. Visc. (Ns/m^2)
1.25E-03	3.94E-12	9.95E-04
2.50E-03	3.14E-12	1.11E-03
5.00E-03	2.86E-12	1.40E-03
7.50E-03	2.71E-12	1.74E-03
1.00E-02	2.03E-12	2.16E-03
1.50E-02	1.57E-12	3.18E-03

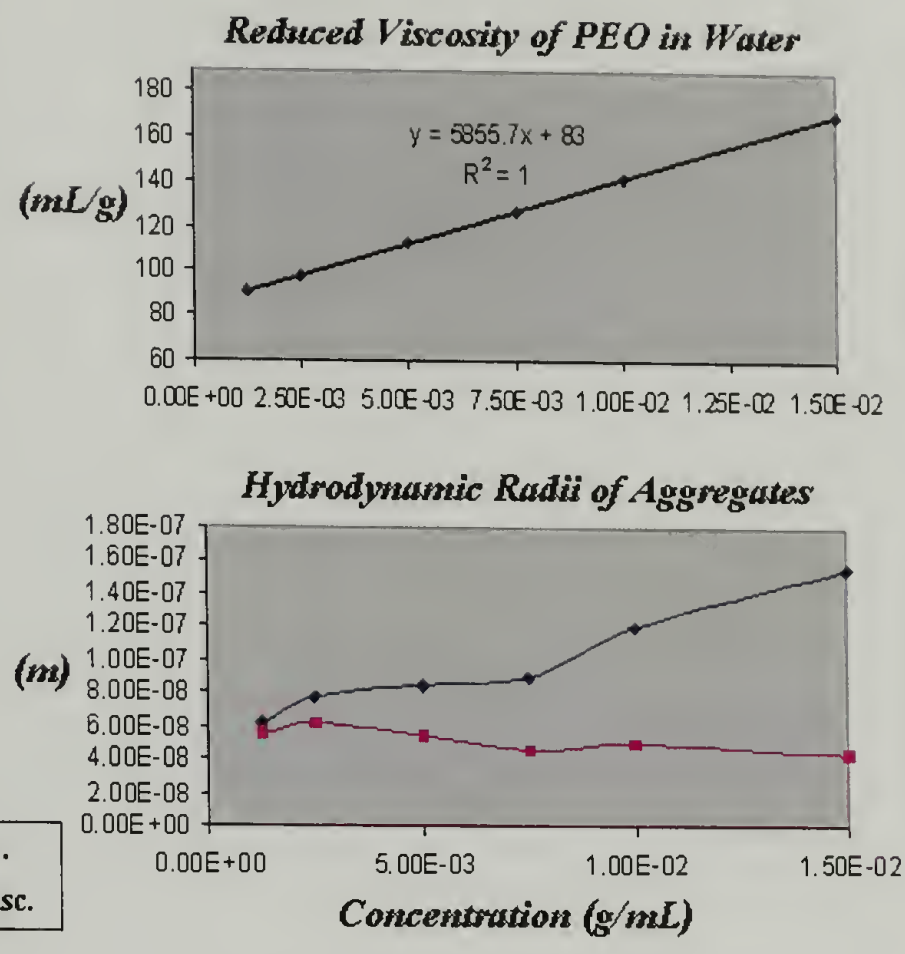

Figure 4.5. Reduced viscosity of PEO in water and aggregate hydrodynamic radii versus PEO concentration. Hydrodynamic radii of 96,000 g/mol PEO aggregates with no added salt calculated with (a) the viscosity of water at 25°C and (b) concentration-dependent viscosity of PEO in water at 25°C.

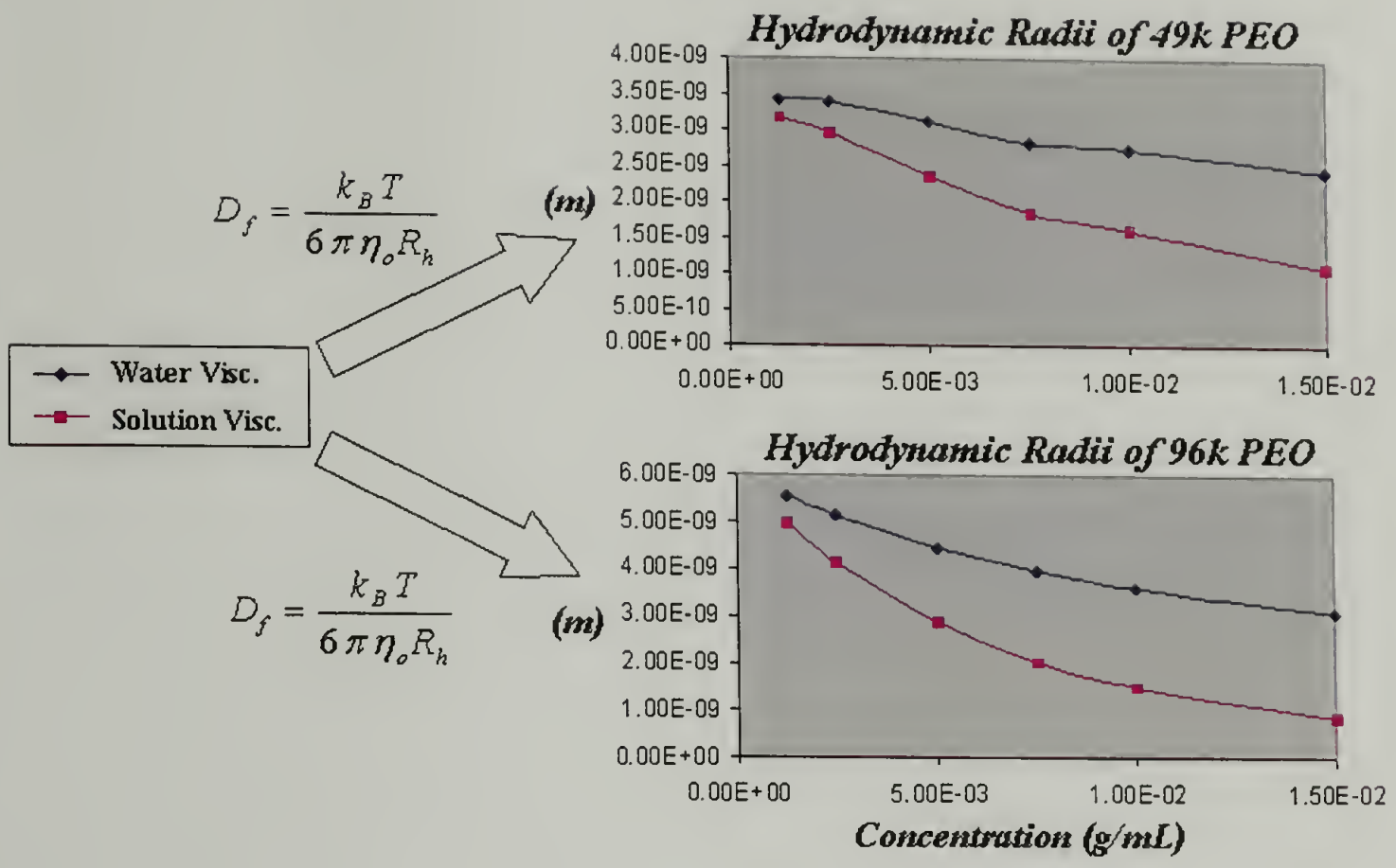

Figure 4.6 Hydrodynamic radii of single chains as a function of PEO concentration. Hydrodynamic radii of 49,000 g/mol and 96,000 g/mol PEO single chains with no added salt calculated with (a) the viscosity of water at 25°C and (b) concentration-dependent viscosity of PEO in water at 25°C.

CHAPTER 5

SUMMARY AND FUTURE DIRECTIONS

5.1 Introduction

Dilute polymer solutions are important in science and technology, spanning concentrations from isolated single chains to solutions approaching overlap concentration (c*). These solutions are ubiquitous in biological systems being found in many extra- and intra-cellular processes. As many body systems, they display numerous fascinating collective phenomenon including growth of highly ordered crystalline phases and formation of aggregates including micelles. They are used in cosmetics, drug-delivery, food processing, controlling the flow of liquids, among other technological applications.

In this thesis, we reported Monte Carlo simulations, Small Angle Light Scattering (SALS) studies and Dynamic Light Scattering (DLS) studies of dilute polymer solutions. Using Monte Carlo techniques, we modeled adsorption of a single chain to a patterned surface. With SALS we studied the kinetics of polyethylene crystallization from organic solvent. Finally, DLS was performed to detect slow mode diffusion of polymer aggregates and measure the associated diffusion coefficients.

5.2 Monte Carlo Simulations

We have performed an extensive set of Monte Carlo simulations of fixed-length charged polymers adsorbing to an assortment of patterned planar charged surfaces. We simulated polymers with a uniform negative block, alternating negative

and neutral blocks (negative/neutral polymers), and alternating positive and negative blocks (positive/negative polymers) adsorbing to stripe and checkerboard surface patterns. The chain entropy associated with polymer loops and twists prevents efficient pattern recognition with the surfaces. The polymer must be able to traverse many meta-stable states to achieve a final strongly absorbed configuration. This process is dictated by the size of the charged surface patterns and their correlation to the size of the charged polymer segments. We found that simply increasing the electrostatic interactions between the polymer segments and the surface patterns is not sufficient to achieve pattern recognition. Effective pattern recognition requires a reduction of loops and twists favored by entropy as well as the ability to desorb from intermediate states. This is achieved by reducing the electrostatic interactions between polymer and surface to a point just above the adsorption threshold. Our results indicate that long runs of one kind of charged polymer block or charged sequence in a surface pattern will, in general, enhance pattern recognition. We found that the positive/negative polymers prefer the positive/negative surfaces when the block size of each is commensurate. The positive/negative charges on the surface will compensate for the positive/negative blocks on the polymer and result in a complete adsorption.

5.3 Small Angle Light Scattering

We have performed kinetic studies of single crystal formation from dilute solution of low-polydispersity polyethylene (PE) in *para*-xylene *in-situ* using SALS. We made multiple measurements varying the quench depth and concentrations for

two different samples of PE. The results for both samples produced asymmetric scattering for the lower temperature quenches to 65°C and symmetric scattering for the higher temperature quenches to 80°C. The crossover from asymmetric to symmetric scattering was smooth as we changed quench depth and was between 70°C and 75°C for the 0.05 wt.% and the 0.1 wt.% solutions. The correlation length corresponding to scattering peak was between 15 and 30 μm for all of our SALS experiments. Our results may indicate assembled regions of crystal platelets in a liquid-crystalline phase for lower temperature quenches. We believe that the crystals nucleating closer together in the deeper quench give rise to ordering that is responsible for the asymmetric scattering.

5.4 Dynamic Light Scattering

We have reported on diffusion studies of single chain and aggregated species of NaPSS and PEO with added $BaCl_2$. We performed these studies with DLS to measure the fast mode (D_{fast}) and slow mode (D_{slow}) diffusion coefficients as a function of polymer concentration. All these measurements were made in the dilute concentration regime. The D_{fast} and D_{slow} was relatively constant for both polymers in our concentration regime, differing by about 1½ orders of magnitude: 1.1×10^{-6} cm^2/s versus 7.8×10^{-8} cm^2/s for NaPSS and 6.7×10^{-7} cm^2/s versus 4.2×10^{-8} cm^2/s for PEO. In addition, we calculated the viscosity of PEO in water as a function of polymer concentration from 1.25 g/L to 15 g/L for two molecular weight samples. We used this concentration dependent viscosity along with D_{fast} and D_{slow} to calculate hydrodynamic radii for single chains and aggregates. We find that adding a divalent

salt like $BaCl_2$ results in a slow mode for both NaPSS and PEO. We also found that PEO aggregated without salt during our sample preparation, and that using a concentration dependent viscosity in the Stokes-Einstein relation resulted in stable aggregate radii in the concentration regime we investigated.

5.5 Future Directions

Possible extensions of our Monte Carlo work could focus on thoroughly investigating positive/negative polymers adsorbing to positive/negative surfaces. Detailed studies are needed of the effects of varying the sizes of charge blocks and their sequences on the adsorption of the polymer to the surface. Also, kinetic studies can be done to follow the time evolution of the polymer traversing meta-stable states along the surface to the final equilibrium state. The position of the polymer segments as a function of time would allow us to watch a movie of the adsorption process.

More detailed SALS studies are needed to pinpoint the exact transition temperature from asymmetric to symmetric scattering as a function of polymer concentration. Other experiments are required to measure the correlation lengths associated with partially stacked or aligned single crystal platelets. SANS and SAXS are possible tools to probe liquid-crystalline ordering in solution that result in structures on the order of two or three crystals thick.

Using DLS to probe aqueous solutions of NaPSS and PEO with added $BaCl_2$ revealed a stable polymer concentration regime with respect to diffusion of aggregates and single chains. This concentration regime may be a good starting point to explore the micellization of NaPSS and PEO diblocks. The size of the micelles that form,

including the core and corona radii, should depend largely on the ionic strength of solution as well as the relative and absolute size of the polymer blocks. DLS can be a powerful tool to probe the formation of these structures.

BIBLIOGRAPHY

[1] M. Muthukumar, Curr. Opin. Colloid Interface Sci. **3**, 46 (1998).

[2] H. Dautzenberg, W. Jaeger, J. Kötz, B. Philipp, Ch. Seidel, and D. Stscherbina, *Polyelectrolytes: Formation, Characterization and Application* (Hanser and Gardner, Cincinnati, 1994).

[3] B. Alberts, D. Bray, J. Lewis, M. Raff, K. Roberts, and J. D. Watson, *Molecular Biology of the Cell* (Garland, New York, 1994).

[4] P. Dubin, J. Bock, R. Davis, D. N. Schulz, and C. Thies, *Macromolecular Complexes in Chemistry and Biology* (Springer, Berlin, 1994).

[5] A. L. Margolin, S. F. Sherstyuk, V. A. Izumrudov, A. B. Zezin, and V. A. Kabanov, European Journal of Biochemistry **146**, 625-632 (1985).

[6] T. Radeva, *Physical Chemistry of Polyelectrolytes* (Marcel Dekker, New York, 2001).

[7] L. Wagberg, L. Winter, L. Odberg, and T. Lindstrom, Colloids and Surfaces **27**, 163-173 (1987).

[8] Y. Adachi, and T. Matsumoto, Colloids Surf., A **113**, 229 (1996).

[9] K. W. Mattison, I. J. Brittain, and P. L. Dubin, Biotechnol. Prog. **11**, 632-637 1995).

[10] A. Tsuboi, T. Izumi, M. Hirata, J. Xia, P. L. Dubin, and E. Kokufuta, Langmuir **12**, 6295-6303 (1996).

[11] Y. Li, P. L. Dubin, H. Dautzenberg, U. Luck, J. Hartmann, and Z. Tuzar, Macromolecules **28**, 6795-6798 (1995).

[12] Y. Li, P. L. Dubin, H. A. Havel, S. L. Edwards, and H. Dautzenberg, Langmuir **11**, 2486-2492 (1995).

[13] H. Zhang, Y. Li, P. Dubin, and T. Kato, Journal of Colloid and Interface Science **183**, 546-551 (1996).

[14] J. L. Thomas, K. A. Borden, and D. A. Tirrell, Macromolecules **29**, 2570 (1996).

[15] P. Haronska, T. A. Vilgis, R. Grottenmuller, and M. Schmidt, Macromol. Theory Simul. **7**, 241-247 (1998).

[16] M. Muthukumar, J. Chem. Phys. **86**, 7230-7235 (1987).

[17] F. v. Goeler and M. Muthukumar, J. Chem. Phys. **100**, 7796-7803 (1994).

[18] C. Y. Kong and M. Muthukumar, J. Chem. Phys. **109**, 1522-1527 (1998).

[19] M. Muthukumar, J. Chem. Phys. **103**, 4723-4731 (1995).

[20] M. Muthukumar, PNAS **96**, 11690-11692 (1999).

[21] A. K. Chakraborty and D. Bratko, J. Chem. Phys. **108**, 1676-1682 (1998).

[22] S. Srebnik, A. K. Chakraborty, and D. Bratko, J. Chem. Phys. **109**, 6415 (1998).

[23] F. Carlsson, P. Linse, and M. Malmstem, J. Phys. Chem. B **105**, 9040 (2001).

[24] A. Baumgärtner, *Applications of the Monte Carlo Methods in Statistical Physics*, edited by K. Binder (Springer, New York, 1984).

[25] P. Welch and M. Muthukumar, Physical Review Letters **87**, 21 (2001).

[26] M. Muthukumar and P. Welch, Polymer **41**, 8833-8837 (2000).

[27] A. Keller and E. Pedemonte, J. Crystal Growth **18**, 111-123 (1973).

[28] S. J. Organ and A. Keller, J. Polymer Sci., B., Polymer Phys. **24**, 2319-2335(1986).

[29] Akihiko Toda, Polymer **28**, 1645-1651 (1987).

[30] E. Riande and J. M. G. Fatou, Polymer **17**, 795-801 (1976).

[31] M. Cooper and R. St. J. Manley, Polymer Letters Edition **11**, 363-367 (1973).

[32] M. Cooper and R. St. J. Manley, Macromolecules **8**, 2, 219-227 (1975).

[33] E. Riande and J. M. G. Fatou, Polymer **17**, 99-104 (1976).

[34] Shouke Yan, Jürgen Petermann and Decai Yang, Polymer Bulletin **38**, 87-94 (1997).

[35] S. Hocquet, M. Dosiere, Y. Tanzawa and M. H. J. Koch, Macromolecules **35**, 5025-5033 (2002).

[36] B. Wunderlich, E. A. James and Tsao-Wen Shu, J. Polymer Sci., A. **2**, 2759-2769 (1964).

[37] Yan Deyue, Chinese Science Bulletin **43**, 7, 564-568 (1998).

[38] R. L. Miller and J. D. Hoffman, Polymer **32**, 6, 963-978 (1991).

[39] T. W. NG, J. Polymer Sci., B., Polymer Phys. **34**, 199-201 (1997).

[40] Ya Peng, Qiang Fu and Fang-Chyou Chiu, Polymer International **52**, 164-171 (2003).

[41] O. V. Borisov and E. B. Zhulina, Macromolecules **35**, 4472-4480 (2002).

[42] E. E. Dormidontova, Macromolecules **35**, 987-1001 (2002).

[43] M. Muthukumar, J. Chem. Phys. **107**, 7, 2619-2635 (1997).

[44] S. Förster and M. Schmidt, Polymer. **31**, 781-792 (1990).

[45] M. Sedlák and E. J. Amis, J. Chem. Phys. **96**, (1), 826-834 (1992).

[46] M. Sedlák, J. Chem. Phys **105**, (22), 10123-10133 (1996).

[47] M. Drifford et al., Ber. Bunsenges. Phys. Chem. **100**, 829-835 (1996).

[48] J. J. Tanahatoe and M. E. Kuil, J. Phys. Chem. B, **101**, 9233-9239 (1997).

[49] W. F. Polik and W. Burchard, Macromolecules **16**, 978-982 (1983).

[50] K. Devanand and J. C. Selser, Nature **343**, 739-741 (1990).

[51] K. Devanand and J. C. Selser, Macromolecules **24**, 5943-5947 (1991).

[52] M. Duval and D. Sarazin, Polymer **41**, 2711-2716 (2000).

[53] M. Duval, Macromolecules **33**, 7862-7867 (2000).

[54] J. K. Armstrong et al., Langmuir **17**, 4482-4485 (2001).

[55] R. Xu and M. A. Winnik, Macromolecules **24**, 87-93 (1991).

[56] L. M. Bronstein et al., Langmuir **15**, 6195-6200 (1999).

[57] S. Förster et al., Macromolecules **35**, 4096-4105 (2002).

[58] H. Vink, Makromol. Chem. **182**, 279-281 (1981).